Q. J. R. Meteorol. Soc. (2000), **126**, pp. 3067–3095

Cloud-resolving simulation of convective activity during TOGA-COARE: Sensitivity to external sources of uncertainties

By F. GUICHARD*, J.-L. REDELSPERGER and J.-P. LAFORE
CNRM/GAME, Météo-France and CNRS, France

(Received 13 January 2000; revised 8 May 2000)

SUMMARY

A one-week convective period of the Coupled Ocean–Atmosphere Response Experiment (10–17 December 1992), prior to a westerly wind burst, has been simulated with a cloud-resolving model. Large-scale advection derived from observations is used to force the model, in the same way as usually done in single-column models. Our aim is to evaluate this explicit simulation against observed large-scale thermodynamic and radiative fields, and to investigate the sensitivity of model results to observational uncertainties. Precipitation, apparent heat source and moisture sink are fairly well reproduced by the model as compared to those diagnosed from observations. Temperature (T) and moisture (q_v) fields are also reasonably well captured except for a moderate cold and moist bias. Simulated moist static energy is too high below 6 km and too low above, possibly because convection is slightly less active in the model than observed.

In order to investigate the sensitivity of model results to observational uncertainties, results are analysed with the moist static energy budget together with independent observational radiative datasets. This analysis suggests that the atmospheric radiative rate that is in equilibrium with the applied large-scale advection and observed surface fluxes is too weak and that its diurnal cycle is not realistic. The most likely reason for this problem is found to be related to uncertainties in the large-scale advection diagnosed from observations. This analysis also indicates that the simulated high-cloud cover is too large in the model. It is greatly improved by increasing the ice-crystal fall speed. Additional tests show a large sensitivity of the simulated moist static energy, and thus T and q_v, to the range of uncertainties previously found for large-scale advection. The vertical structure of the model bias is not significantly modified by changing the intensity of these forcings, but it is most sensitive to their vertical structures.

It is argued that it is crucial to get some insights into the range of uncertainties of external forcings (large-scale advection, surface fluxes and atmospheric radiative-heating rate) so as to assess the relevance of any evaluation of simulated temperature and moisture when a model, either resolving clouds or parametrizing them, is forced with large-scale advection deduced from observations.

KEYWORDS: Cloud-resolving models Clouds GCSS TOGA-COARE

1. INTRODUCTION

An accurate representation of the impact of convective cloud systems on their environment is a crucial issue for weather-forecast and climate models. Though many studies have been devoted to this topic, a better understanding of convective cloud systems is still required, in particular in the Tropics, in order to further improve our knowledge of large-scale dynamics and budgets at these latitudes (Hartmann *et al.* 1984; Gregory 1997). Deep convective systems are important because they affect their environment through strong latent-heat release and vertical redistribution of temperature, water vapour and momentum. They also play a significant role in the radiative budget, directly through temperature and water-vapour vertical redistributions but also via the radiative impact of convectively generated clouds, for instance the large tropical anvils (e.g. Del Genio *et al.* 1996). Furthermore, convective systems also impact the ocean through their impact on the surface heat and stress fluxes (Godfrey *et al.* 1998; Redelsperger *et al.* 2000a).

At mesoscale, cumulus cloud ensembles appear as complex nonlinear atmospheric features involving various processes—turbulence, large-scale motion, microphysics and radiation—that take place and strongly interact *at smaller scale than currently resolved by large-scale models*. Various cumulus schemes have been developed, aiming at

* Corresponding author: CNRM/GAME, 42 Av. Coriolis, 31057 Toulouse Cedex 1, France.
e-mail: francoise.guichard@meteo.fr

representing these small-scale convective processes, and major effort has been devoted to their improvement in the past 20 years.

An important part of the testing and evaluation of cumulus schemes relies on validations of model results against large-scale budgets derived from observations. In this approach, the behaviour of a parametrization is investigated with a single-column model (SCM) (e.g. Lord 1982; Bougeault 1985; Tiedtke 1988; Emanuel and Zivkovic-Rothman 1999). This framework allows spurious large-scale feedbacks to be eliminated—the large-scale forcings are prescribed—and to test the scheme under more realistic conditions than usually encountered in a full large-scale model. For instance, large-scale budget datasets obtained during GATE (GARP* Atlantic Tropical Experiment) (Thompson *et al.* 1979), and the Tropical Ocean Global Atmosphere Coupled Ocean–Atmosphere Response Experiment (TOGA-COARE) (Webster and Lukas 1992; Lin and Johnson 1996a) have frequently been used for this purpose.

Similar experiments can now be performed with cloud-resolving models (CRMs), which are able to explicitly simulate deep convective cells and surface–convection–microphysics–radiation interactions. Therefore, CRMs can provide datasets documenting cloud-related processes and statistics not obtained from observations alone, though crucial for testing the hypothesis underlying convection schemes and improving them (e.g. Gregory and Miller 1989). In fact, an important part of GCSS (GEWEX† Cloud System Study) (Browning *et al.* 1993) strategy now relies on the use of CRMs for providing relevant findings and data in order to improve cumulus parametrizations (e.g. Moncrieff *et al.* 1997; Redelsperger *et al.* 2000b).

In this GCSS framework, a westerly wind burst (WWB) period of COARE (20–26 December 1992) has been used as a common case for both CRM and SCM intercomparison studies (Krueger 1997). In the present study, a cloud-resolving model is used to simulate a one-week convective period of COARE (10–17 December 1992), prior to this westerly wind burst. It is difficult for a general-circulation model (GCM) to reproduce these events; it is also crucial, as WWB triggering is a key component of the west Pacific climate (e.g. Godfrey *et al.* 1998). As seen later, this transition period is also quite contrasted with the WWB period in terms of moisture. The framework of the simulation is similar to Grabowski *et al.* (1996) or Xu and Randall (1996). They performed CRM simulations of the GATE area over a week or more, using prescribed large-scale advection evolving with time, and nudging winds towards observed. In fact, almost twenty years ago Soong and Tao (1980) introduced this approach with a CRM, but over a smaller domain and shorter time-scale. Using COARE data, Wu *et al.* (1998, 1999) and Li *et al.* (1999) were also able to simulate the convective activity over the COARE area with two-dimensional CRMs. These studies have focussed in particular on the quality of simulated temperature and moisture fields, as these fields reflect the proper behaviour of convection in the model—as long as the other processes are well represented. CRM simulations of the GATE area have been more successful at reproducing observed temperature and moisture fields than the one of the COARE Intensive Flux Array (IFA). It has been shown also that these results were sensitive to the microphysical and radiative parametrization, but it is not always clear that better results are linked to improved physical parametrizations (Li *et al.* 1999). Grabowski *et al.* (1996), and then Wu *et al.* (1998) argued that the lack of large-scale advection of long-lasting ice anvils in their forcing dataset was partly responsible for the discrepancies between simulated

* Global Atmospheric Research Program.

† Global Energy and Water Cycle Experiment.

and observed thermodynamic fields, whereas Emanuel and Zivkovic-Rothman (1999) argued that errors in the large-scale forcings play a role too.

Indeed, before explicitly addressing specific issues related to convective parametrizations in using CRM datasets, it is important and necessary to evaluate model results. Thus, the main goal of this study is to evaluate the simulation against observed large-scale thermodynamic and radiative quantities. In addition, sensitivity tests on possible sources of uncertainties are discussed in detail. The sensitivity of the thermodynamic fields to the solid-hydrometeor fall speed and the accuracy of the large-scale tendencies is specially analysed. A detailed analysis and discussion of thermodynamic budgets and cloud statistics for this case (similar to Guichard *et al.* 1997b), relevant to convection parametrization issues, will be the subject of a following paper.

The present paper is organized as follows. The design of the experiment is presented in section 2. An evaluation of model performances is given in section 3, focussing on convective features and thermodynamic profiles. These results are further discussed by contrasting different observational datasets in section 4. The implications of observational uncertainties on the model evaluation are investigated in section 5.

2. Model and experimental design

(*a*) *The model*

The simulations are performed with the anelastic non-hydrostatic cloud-resolving model of Redelsperger and Sommeria (1986). This model has been extensively used over a wide range of scales to represent squall lines (Lafore *et al.* 1988), frontal systems (Redelsperger and Lafore 1994) and shallow convection. Its main characteristics are listed in the following.

Model prognostic variables are the three components of the wind, u, v and w, the potential temperature θ, the specific humidity q_v, mixing ratios for five hydrometeor species (cloud liquid droplets q_c, rain drops q_r, ice crystals q_i, aggregates q_n and graupel q_h) and the subgrid turbulent kinetic energy e_t. A Kessler-type parametrization is used for warm microphysical processes, except for subgrid-scale condensation and conversion from cloud droplets in raindrops (Redelsperger and Sommeria 1986). Ice-phase microphysics is treated with the scheme developed by Caniaux *et al.* (1994), including three prognostic equations for the following solid hydrometeors: ice crystals, aggregates and graupel. Special care has been given to the formulation of parametrized turbulent processes. Based on a prognostic equation for e_t, it uses quasi-conservative variables for condensation and incorporates the effect of thermal stratification on subgrid fluxes (Balaji and Redelsperger 1996).

Radiative effects are computed fully interactively with the cloud field using the radiation scheme of the European Centre for Medium-Range Weather Forecasts (ECMWF) (Morcrette 1991; see Guichard *et al.* 1996 for its implementation in the CRM). Radiative fluxes are computed every minute and every 15 min for cloudy and clear-sky columns, respectively. Ice-cloud properties are parametrized following Ebert and Curry (1992) and Smith and Shi (1992), with an effective radius fixed at 40 μm for ice crystals.

(*b*) *Selected period*

The four months of the Intensive Observing Period (IOP) of COARE exhibit various periods of wind regime and convective activity (Lin and Johnson 1996a,b). In particular, the IFA of COARE is characterized by a weak wind shear, except during the three WWBs. As an example, Fig. 1 shows, for the whole month of December 1992, the

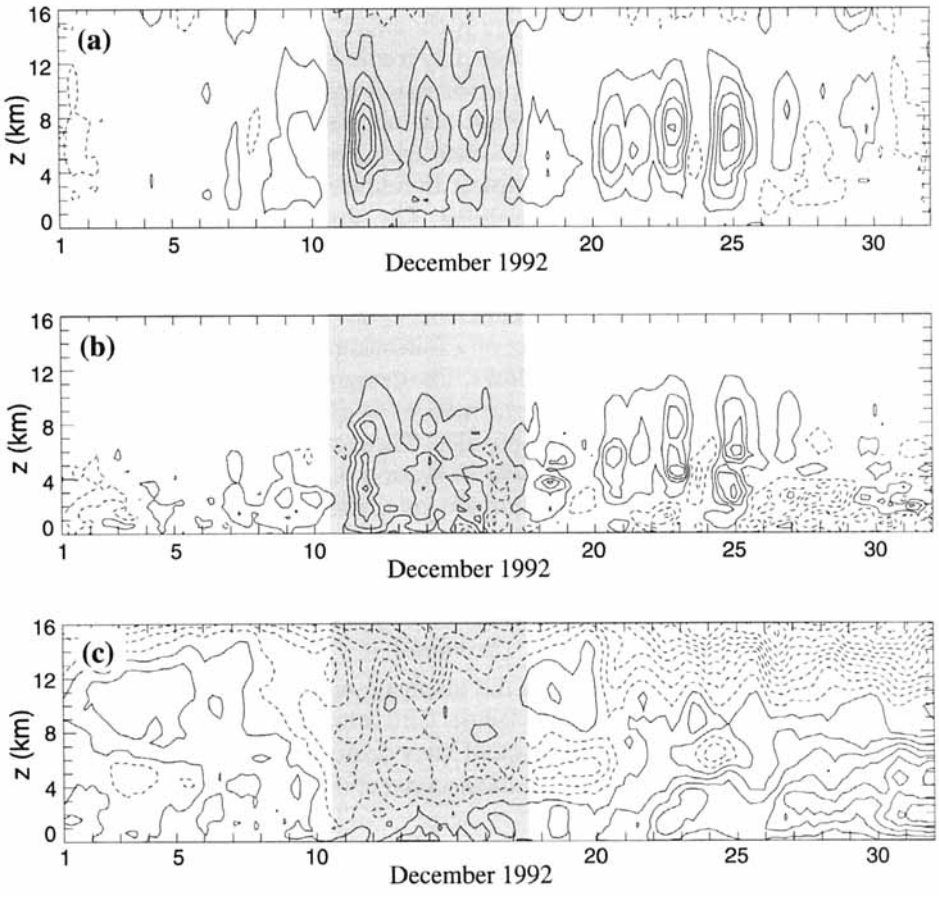

Figure 1. Eighteen-hour running mean: (a) apparent heat source Q_1, (b) moisture sink Q_2, and (c) zonal wind U over the IFA for the month of December 1992 diagnosed from observations (Ciesielski *et al.* 1997). The contour interval, lower and higher isolines are, respectively, 5 K d^{-1}, -2.5 K d^{-1} and 25.5 K d^{-1} for Q_1, 5 K d^{-1}, -12.5 K d^{-1} and 17.5 K d^{-1} for Q_2, and 3 m s^{-1}, -33 m s^{-1} and 18 m s^{-1} for U. The shading marks a period of intensive convective activity.

mean apparent heat source Q_1, apparent moisture sink Q_2 and zonal wind over the IFA as deduced from the sounding network of TOGA-COARE by Ciesielski *et al.* (1997).

The period 20–26 December 1992 chosen for the second case of the GCSS Working Group 4 (WG4) model intercomparisons project (Krueger 1997) corresponds to the WWB onset (Fig. 1(c)). The present paper focusses on the 10–17 December 1992 period of intense convective activity which occurred prior to this WWB (shaded zone in Fig. 1). Vertical structures of Q_1 and Q_2 are different for these two periods. For the pre-WWB period, the height of Q_1 maxima lies around 7 km, whereas Q_2 maxima are located lower, around 4 km. For the WWB period, differences between the height of Q_1 and Q_2 maxima were much weaker. Drying also occurred in the low levels during the pre-WWB period in contrast to the WWB period. These features can be related to the characteristics of convective systems. Satellite observations indicate that the size of convective systems and their associated stratiform parts are less extended during the pre-WWB period than during the WWB period. As shown in Redelsperger and Guichard (1996) for instance, both convective and stratiform parts of cloud systems contribute significantly to the total

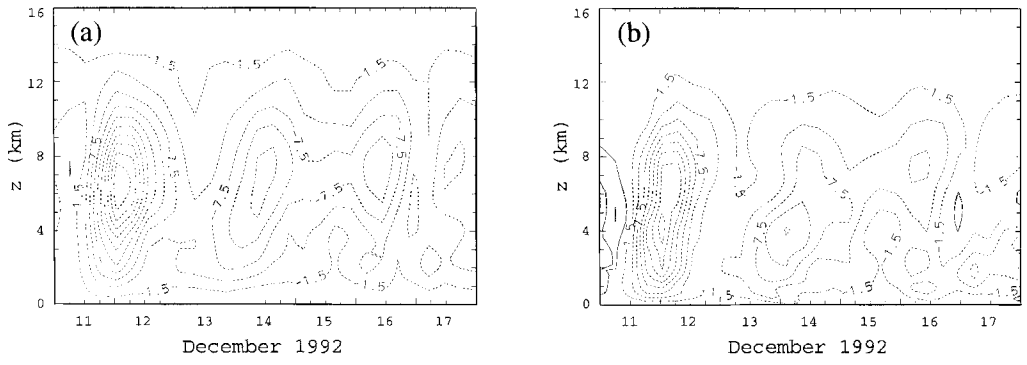

Figure 2. Temporal evolution of the forcing of (a) temperature and (b) moisture by the large-scale motions. The contour interval is 3 K d^{-1} and the time average is 6 h.

Q_1 and Q_2. By their nature they also impact very differently on the vertical structure of Q_1 and Q_2. Therefore, convective systems characterized by a different ratio of their respective area occupancy might lead to different structures of Q_1 and Q_2 similar to observed.

(c) *Model set-up*

The simulation is performed in two-dimensions (2D), due to the tremendous cost of three-dimensional (3D) simulations over a whole week. Moreover, a comparison of 2D and 3D simulations by Grabowski *et al.* (1998) shows that a 2D framework is suitable for deep-convection simulation when, as for the present study, the large-scale forcings are prescribed and the mean wind is nudged towards the observed large-scale wind. The domain size is 512 km along the horizontal axis and 23 km in height. The horizontal grid spacing is 2 km. The vertical grid is stretched, from 70 m resolution in the lower layers up to 700 m above 10 km. A sponge layer is added above the tropopause, between 16 and 23 km, to avoid spurious reflections. A time step of 12 s is used and the model integration is done for seven days of physical time. The simulation starts at 1200 UTC 10 December 1992 from horizontally homogeneous profiles corresponding to IFA mean values derived by Ciesielski *et al.* (1997).

Cyclic lateral-boundary conditions are used, so that the forcing of temperature and water vapour by the large-scale motion is introduced as an additional term. Following Sommeria (1976), it is applied homogeneously to each column of the simulated domain, as a function of height and time only (see also Grabowski *et al.* 1996). The sum of large-scale horizontal and vertical forcings deduced from observations every six hours is linearly interpolated between two consecutive dates. Large-scale vertical advection is the dominant contributor to the total forcing. However, horizontal advection of water vapour is not negligible, and usually dries the domain, mostly around 4–5 km (not shown). Temporal evolution of these forcings are presented in Fig. 2. During this period, the large-scale thermodynamic forcing consists mainly in a cooling and moistening of the atmosphere. As previously noted for Q_1 and Q_2, the large-scale advection of heat and of moisture exhibit different vertical structures: maxima of large-scale cooling are located around 6 km, whereas the large-scale moistening usually peaks at lower heights, around 4 km.

The large-scale wind is important, as cloud organization, involving cloud-system propagation and structure (e.g. squall, non-squall lines), is strongly linked to mean wind

and wind-shear fields. Here, horizontal mean winds are nudged towards observed large-scale values, with a relaxation time of 2 h. For the period under study, the mean zonal-wind shear is relatively weak (Fig. 1(c)), westerly below 2 km, and easterly above, with moderate surface values of the order of a few m s^{-1}.

The sea surface temperature (SST) is prescribed in the simulation, by linearly interpolating the 6 h sampled IFA mean SSTs provided by Lin and Johnson (1996b) and Weller and Anderson (1996). During this seven-day period, SST is of the order of 303 K. It progressively decreases from 303.3 K down to 302.5 K at the end of the seventh day.

3. Comparison with observations: a first evaluation

This section aims at evaluating the simulation of convective features, including rainfall rate, Q_1 and Q_2, and thermodynamic fields.

(*a*) *Precipitation, Q_1 and Q_2*

Figure 3 shows time series of precipitation rate deduced from model and observations. One must keep in mind that the precipitation rate deduced from observations is not a direct measurement, but a residual diagnosed from large-scale thermodynamic budgets and surface evaporation over the IFA, assuming an equilibrium between the vertical integral of the apparent moisture sink Q_2, precipitation and surface evaporation.

Simulated precipitation shows both low and high temporal frequency fluctuations of convective activity, the latter corresponding to the life cycle of deep convective cells. Six-hour mean simulated rainfall is in good agreement with estimations from the budget residual (Johnson and Ciesielski 2000). This is true both in terms of temporal fluctuations and mean rate—with seven-day-mean values of 17.4 and 18.0 mm d^{-1} for simulation and observations, respectively (Fig. 3). This fairly close agreement is not surprising, given the fact that the same large-scale advection is used to deduce a residual rainfall rate and to force the model. It reflects that the assumption used to retrieve the rainfall residual is supported by the model results, at least at first order over time-scales of 6 h or more.

Several low-frequency peaks of precipitation occur, both in the simulation and observations, associated with the maxima of large-scale forcings (Fig. 2). Differences between the two curves are partly rooted in the hypothesis underlying the two rainfall-rate estimates. For instance, simulated spatial variability is related to previous convective activity only, as the large-scale forcing is horizontally homogeneous. This limits the number of mechanisms for convection triggering and inhibition. Estimation of rainfall rates from large-scale observations has other limitations, especially in cases of weak convective activity and on short time-scales. For instance, it leads to a slightly negative value of the rainfall rate at 1200 UTC 16 December.

Finally, a comparison with other sources of observations, such as radar measurements (Short *et al.* 1997), optical rain gauges or retrievals from satellite data (Ebert and Manton 1998) is not straightforward, especially over short time-scales. Indeed, these various observational data do not really cover the same area, and significant discrepancies still exist between these estimates (of the order of 30%) . For instance, radar rainfall products provide estimates over a domain covering approximately half of the IFA. They also show that the spatial variability of surface rainfall is large (Short *et al.* 1997); two adjacent 1° width grid cells can exhibit 20-day-mean rainfall-rate differences of more than 30%. Thus it is not surprising that radar rainfall data—available only for the last two days of simulation—indicate more than twice the IFA-mean residual value. A good

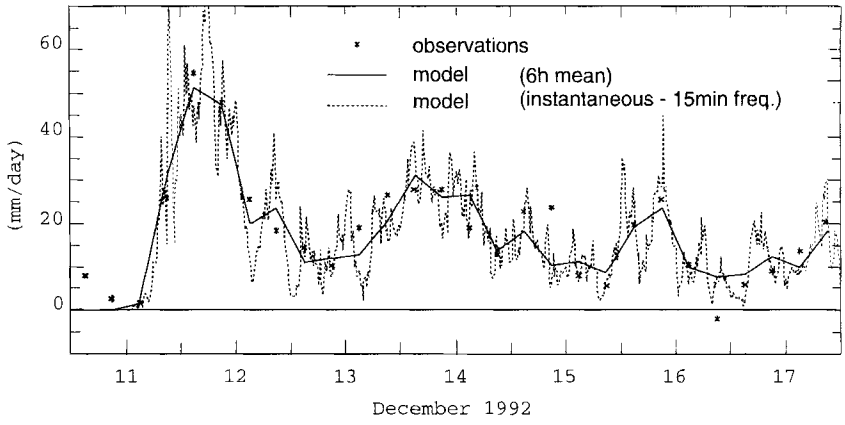

Figure 3. Time series of precipitation rate: deduced from observations with a 6 h frequency (Ciesielski *et al.* 1997), and simulated.

reason for this discrepancy is that most of the convective activity was concentrated in the vicinity of the radar, but did not extend to the whole IFA region.

Model produced Q_1 (Q_1^{mod}) also compares well with Q_1 diagnosed from observations (Q_1^{obs}) (see Figs. 4(a) and (c)). Both display similar vertical structure and temporal fluctuations. Some discrepancies (Fig. 4(e)) occur at high levels where simulated Q_1^{mod} exhibits a stronger diurnal variation. This can be explained by the presence of too many high clouds in the simulation, as will be discussed in section 5. The simulated apparent moisture sink (Q_2^{mod}) also compared favourably with observations, although not to the degree of Q_1^{mod} (Figs. 4(b), (d) and (f)). Synthesized information is given in Fig. 5, showing seven-day-mean average profiles of these fields; Q_1 exhibits a marked maximum around 7 km of the order of 9–10 K d^{-1}, whereas Q_2 is almost constant between 2 and 8 km, uniformly drying the atmosphere by 5 K d^{-1}. Both structures are quite well captured by the CRM. Indeed, over this time-scale, differences are extremely small, of the order of a few tenths of K d^{-1}. Simulated Q_1 and Q_2 are both slightly too weak over the whole column, a feature that is partly due to simulated convective activity being much weaker than observed during the adapting stage (first 12 h of simulation).

These profiles are tightly coupled to the structure of large-scale forcings. Indeed, Eulerian tendencies of temperature and moisture represent a second-order residual between these forcings and the convective response, i.e. both the observed and the simulated atmosphere are in a 'quasi-equilibrium' state. As large-scale vertical advection explains most of the forcing, Q_1 and Q_2 profiles are strongly related to prescribed large-scale vertical gradients of temperature and moisture and large-scale mass fluxes.

(*b*) *Temperature and water vapour*

It is essential that the model reproduces Q_1 and Q_2 correctly, as they determine the resulting profiles of temperature and water vapour, once large-scale motions and surface fluxes are known. Indeed, a relatively small bias of 0.5 K d^{-1} for Q_1 or Q_2 (to be compared with values of Q_1 and Q_2 of the order of 10 K d^{-1}) would lead to a difference of 3.5 K (or 1.33 g kg^{-1}) after seven days. A good agreement of simulated T and q_v with observations is therefore more challenging.

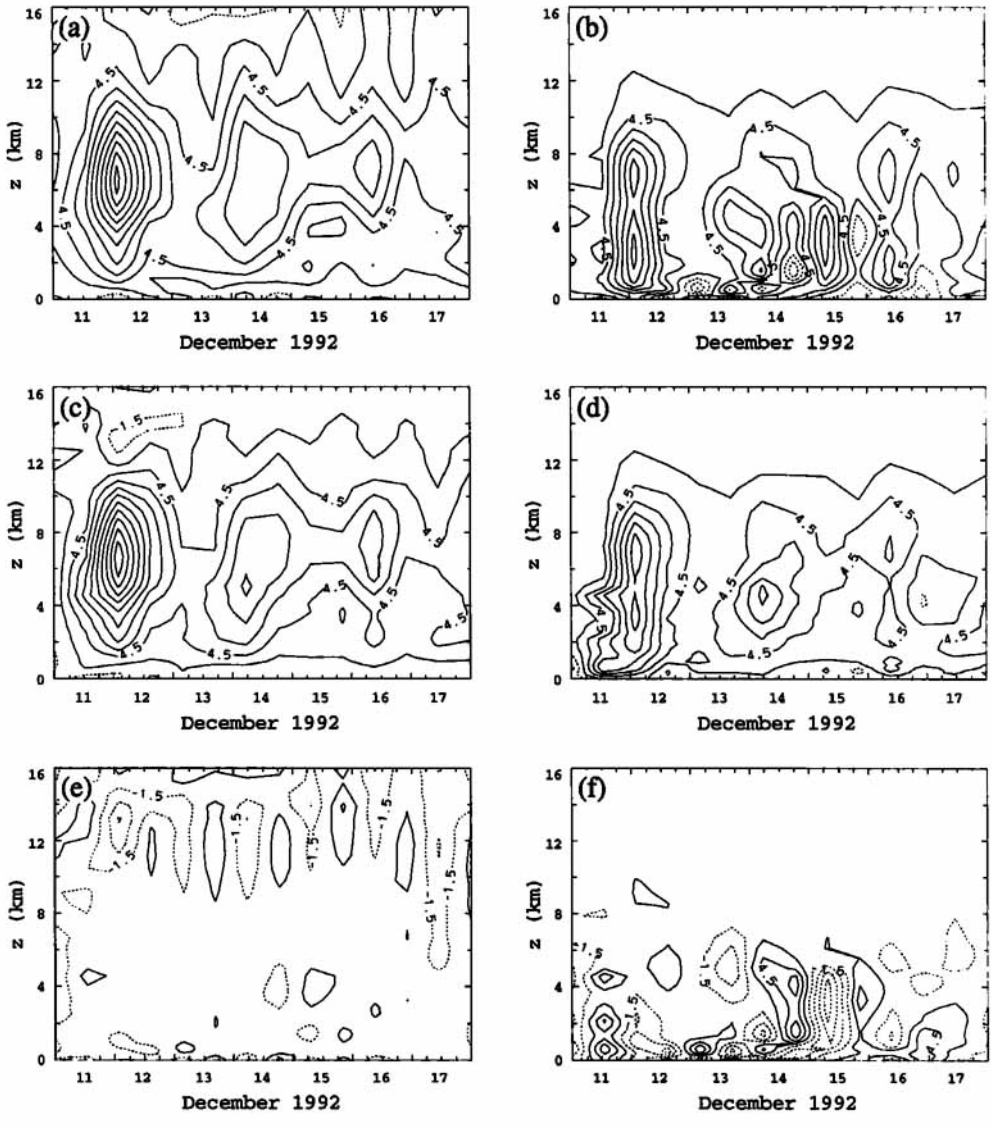

Figure 4. Temporal evolution of (a) the apparent heat source Q_1 and (b) apparent moisture sink Q_2 diagnosed from observations, (c) and (d) simulated Q_1 and Q_2, and (e) and (f) differences between simulated and observed. The contour interval is 3 K d^{-1} starting from the 1.5 isoline (not the zero isoline) and the time average is 6 h.

Simulated temperature agrees fairly well with observed, although overall slightly lower (Fig. 6(a)). The warm bias occurring above 15 km is probably due to a smoothing of the tropopause by the model. Simulated temperature becomes lower than observed in the early stage of the simulation, the difference reaching 1 K within a 12 h period. This is related to the adapting stage occurring in the model. In effect, the model starts from homogeneous conditions, i.e. without any pre-existing spatial variability. Related to this lack of horizontal variability, precipitating convection is delayed by approximately 12 h. During this stage the large-scale forcing induces a significant cooling that is not compensated by any significant warming associated with moist convection; this contrasts with what can be deduced from large-scale observations. After this phase,

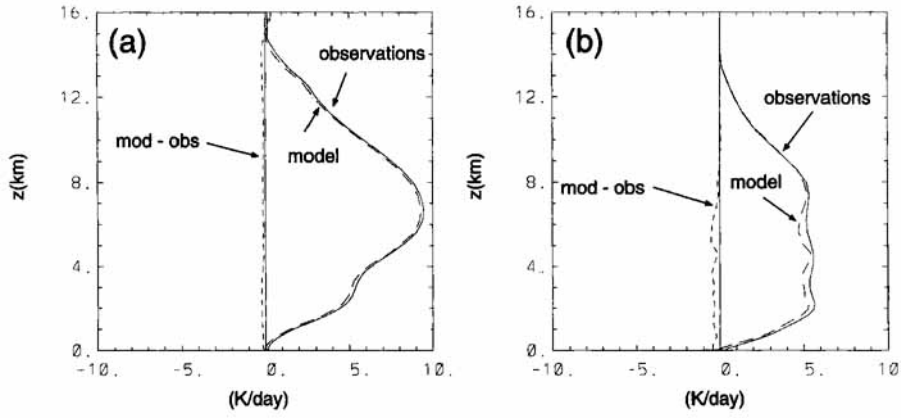

Figure 5. Seven-day-mean profiles of (a) Q_1 and (b) Q_2 (see text), diagnosed from observations (solid line), simulated (short dashes), and the difference 'simulation minus observation' (short dashes).

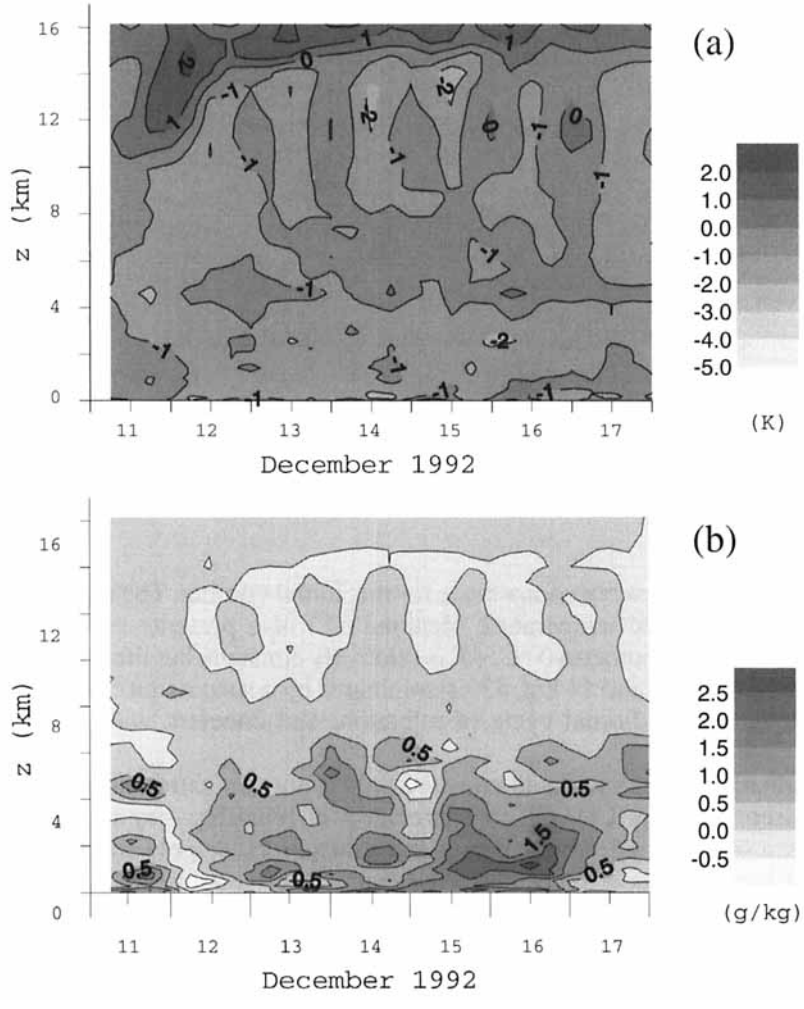

Figure 6. Difference between simulated and observed: (a) temperature T and (b) specific humidity q_v. The contour intervals are 1 K and 0.5 g kg^{-1}, respectively, and the time average is 6 h.

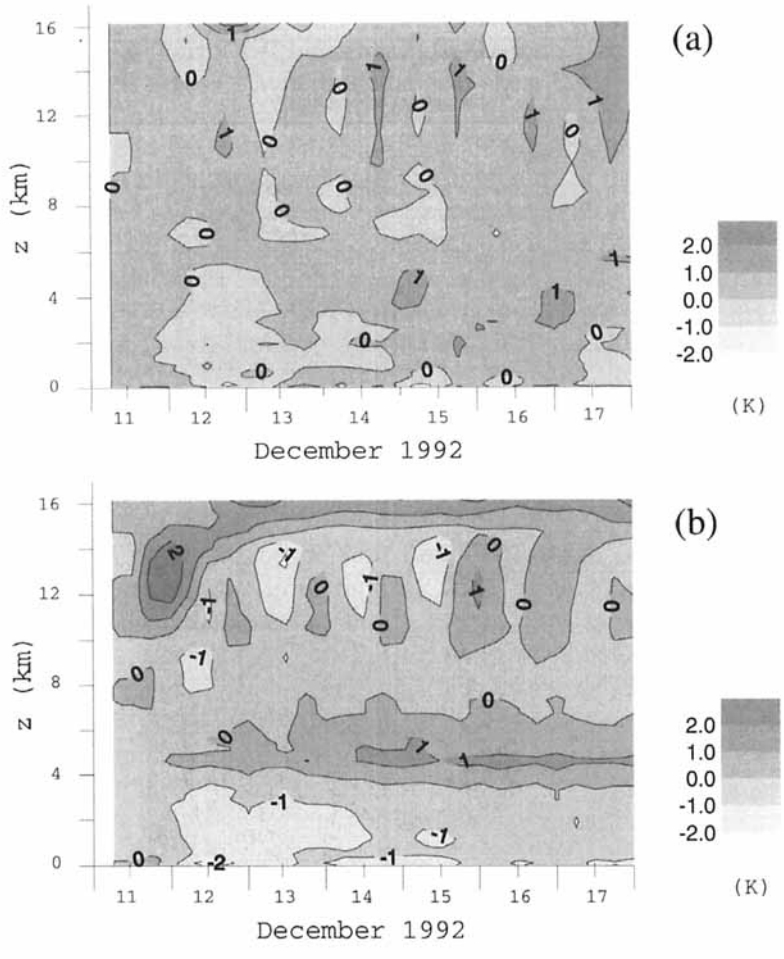

Figure 7. Difference between temperature and initial temperature: (a) observed and (b) simulated. The contour interval is 1 K and the time average is 6 h.

however, the model does not compensate for this initial cooling. The difference between simulated and observed temperature (denoted δT) also presents vertical and diurnal structures. Below the isotherm 0 °C, δT is relatively constant, but then decreases around that height. Between 7 and 14 km, δT is dominated by a succession of isolated extrema, clearly related to the diurnal cycle of radiation, and coherent with previous finding for Q_1.

An evaluation of the simulated moisture field is not straightforward. In effect, it was recently discovered that COARE measurements of humidity—by radiosondes—were affected by a significant dry bias (Zipser and Johnson 1998; Cole and Miller 1999). At the present time the whole set of corrected data is not available, but existing corrected data (Lucas and Zipser 2000; Guichard *et al.* 2000) suggest that the moist bias found in the simulation (Fig. 6(b)) partly reflects an instrumental dry bias. Above 5 km, a comparison of relative humidity RH indicates that simulated RH is larger than observed data by 10 to 20% (not shown). At high levels, RH is tightly coupled to the differences of specific humidity between model and observations. Therefore, the dry bias in RH measurements, which is very high at low temperature (Miloshevich *et al.* 2000), may

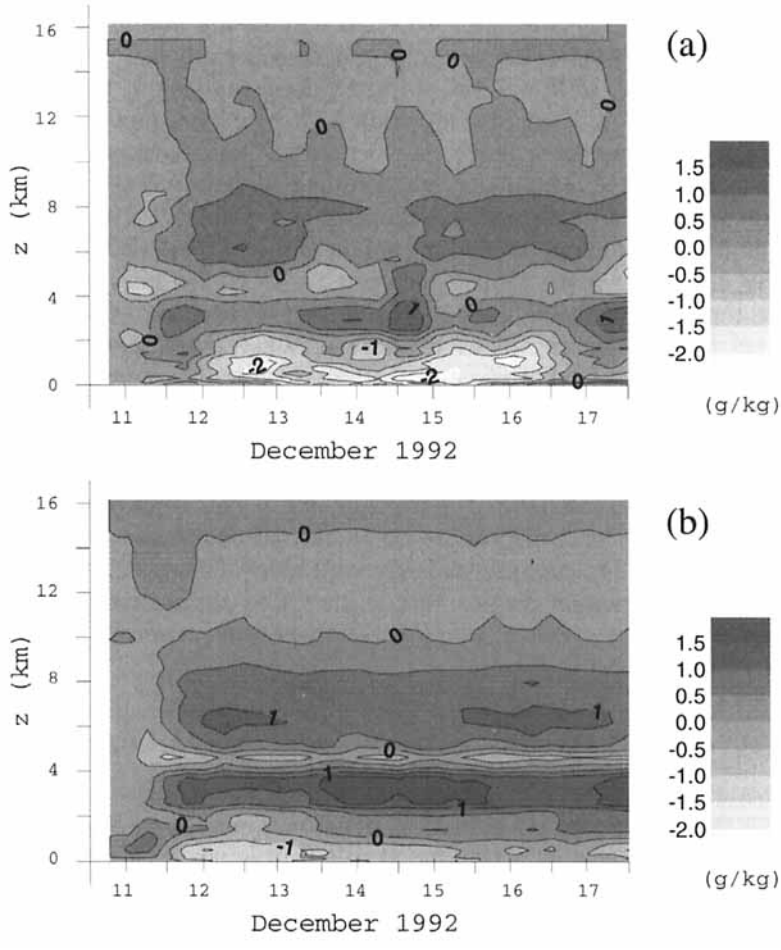

Figure 8. Same as Fig. 7 except for specific humidity. The contour interval is 0.5 g kg^{-1}.

also lead to an overprediction of this simulated moisture bias in the upper levels. In short, the simulated moisture field is probably too moist, but not to the degree indicated by the uncorrected data.

A comparison of the temporal fluctuations of simulated and observed temperature and specific humidity gives some insight into how these fields agree or differ from observations. Observed temperature shows very small temporal deviations, although the first three days appear to be slightly colder and the last four days warmer (Fig. 7(a)). It is also modulated by the diurnal cycle, especially above 10 km. These features are obvious in the simulation too (Fig. 7(b)). The model also develops a structure departing somehow from observations around the height of the isotherm 0 °C, probably associated with the treatment of microphysical processes, including the relatively coarse resolution at these heights (~500 m).

Temporal fluctuations of observed moisture correspond to differences of dry biased profiles (not to their absolute values), spatially averaged moreover. Thus, it can be expected that these fluctuations are less affected by the measurement errors than the moisture profiles themselves. Contrasting with temperature, observed specific humidity (Fig. 8(a)) exhibits much stronger temporal and vertical variations. The convective

events taking place over the IFA are associated with strong drying of the lower levels and considerable moistening of the free troposphere. More precisely, four vertical layers are identified: [0, 2 km], [2 km, 4 km], [4 km, 5 km] and [5 km, 10 km]. Two strong drying phases occur below 2 km, in association with the intense precipitating convective systems. Moistening takes place above, between 2 and 4 km, i.e. approximately up to the height of the isotherm 0 °C. Maxima of moistening tend to occur a few hours before low-level drying (e.g. at the beginning of the second day of simulation), simultaneously with maxima of large-scale forcing. Around the height of the isotherm 0 °C is another drying layer. Finally, the upper layer located between 5 and 10 km becomes moister at the same time as the lower layer ([0, 2 km]) is evolving toward dryer values. Thus, maxima of upper-level moistening do not occur simultaneously with maxima of convective activity, but several hours later. This vertical structure is well captured by the simulation (Fig. 8(b)), but the drying below 2 km is weaker. It is worth noticing that this moist bias is not an intrinsic characteristic of the model, as a similar simulation over the 20–26 December period (GCSS WG4 Case 2) did not exhibit such a strong bias (Fig. 4 of Guichard *et al.* 1997a, and also Fig. 2 of Krueger 1997). This latter period, characterized by much stronger wind shear, did not present intense drying phases either.

Overall, the simulation reproduces fairly well many features of the observed convective activity. An important feature, relevant to GCM parametrization issues, is that the boundary-layer recovery after strong convective events is similar in the simulation and the observations.

4. Assessing the accuracy of external forcings

The previous analysis portrays a simulated atmosphere somehow too cold and moist. This suggests that the convective activity is not strong enough in the model. However, other factors are likely to play a significant role in this result. It is the object of this section to further investigate how the accuracy of 'external forcings' (from the surface, the large-scale motions and the radiative processes) may impact differences between observed and simulated thermodynamic fields.

(*a*) *The moist static energy budget*

Hereafter, our main aim is: (i) to quantify the different forcings, (ii) to evaluate how they differ between observations and simulations and (iii) to get some insights concerning the range of uncertainties from different observational sources. Following Emanuel and Zivkovic-Rothman (1999), we use the moist static energy h ($= c_p T + gz + L_v q$) budget, where c_p is specific heat at constant pressure, g is the gravitational acceleration and L_v is the latent heat of vaporization of water. Indeed, h is not modified by convective processes once integrated over the whole column. The budget is expressed as:

$$\int_0^{p_{\mathrm{srf}}} \frac{\partial h}{\partial t}\frac{\mathrm{d}p}{g} = -\int_0^{p_{\mathrm{srf}}} \left(\frac{\partial \overline{\omega' h'}}{\partial p}\right)\frac{\mathrm{d}p}{g} + \int_0^{p_{\mathrm{srf}}} \left(\frac{\partial h}{\partial t}\right)_{\mathrm{LS}}\frac{\mathrm{d}p}{g} + \int_0^{p_{\mathrm{srf}}} c_p Q_{\mathrm{R}}^p \frac{\mathrm{d}p}{g}. \quad (1)$$

In this equation, p is the pressure, Q_{R}^p the radiative-heating rate and $\overline{\omega' h'}$ the turbulent flux of h. The subscripts 'srf' and 'LS' refer to the surface and the large-scale forcing, respectively. Horizontal turbulent fluxes of h have been neglected and it has been assumed that

$$\int_0^{p_{\mathrm{srf}}} (Q_1 - Q_{\mathrm{R}}^p)\frac{\mathrm{d}p}{g} = \int_0^{p_{\mathrm{srf}}} Q_2 \frac{\mathrm{d}p}{g},$$

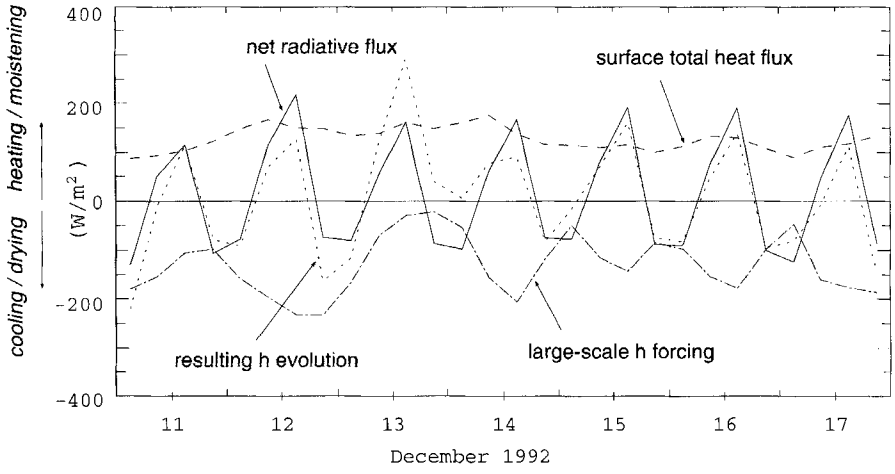

Figure 9. Vertically integrated budget of simulated moist static energy h: temporal evolution (dotted line), surface heat flux (dashed line), large-scale forcing (dashed-dotted line) and net atmospheric radiative flux Φ_R^{mod} (solid line). The time average is 6 h, centred on $(3 + 6n)$ h.

i.e. the net latent-heat release by solidification and fusion is neglected.

In defining the vertical integral $\overline{\overline{h}} = \int_0^{p_{srf}} h \frac{dp}{g}$, representing the mass-weighted average over the vertical column, Eq. (1) can be rewritten

$$\frac{d\overline{\overline{h}}}{dt} = \Phi(h)_{srf} + LS(h) + c_p \overline{\overline{Q_R^p}}, \tag{2}$$

where $\Phi(h)_{srf}$ and $LS(h)$ are the surface flux of h and the mean large-scale advection of h, respectively; $c_p \overline{\overline{Q_R^p}}$ is the net radiative flux into the atmospheric column and will be denoted Φ_R in what follows.

In practice, we have limited the vertical integration to 100 hPa. Large-scale forcings are not available above this height, and their contribution is expected to be much weaker than below. The same is true for radiation.

(*b*) *Analysis of the external forcings*

In the simulation, the large-scale forcings are prescribed. Therefore, the simulated budget can depart from the one diagnosed from observations only through differences in the surface heat fluxes and net atmospheric heating rate. Figure 9 shows the simulated moist static energy budget. The three external forcings (radiative fluxes, surface heat fluxes and large-scale forcing) have the same order of magnitude ($\approx$100 W m^{-2}), but distinct temporal variations. The surface heat flux is the most uniform over the period. It is partly balanced by the large-scale motions which decrease $\overline{\overline{h}}$. The advection shows complex temporal fluctuations, including diurnal modulation during the last four days. The radiative flux, Φ_R^{mod}, does show a consistent diurnal cycle with a weak net effect (15 W m^{-2} on average over the whole period). Resulting temporal variations of h are strongly modulated by Φ_R^{mod}.

A similar budget is derived from the observations (Fig. 10(a)), by coupling large-scale forcings of Ciesielski *et al.* (1997) with observed surface fluxes from Weller and Anderson (1996). In that case, the radiative flux Φ_R^{bud} is the 'residual' that closes

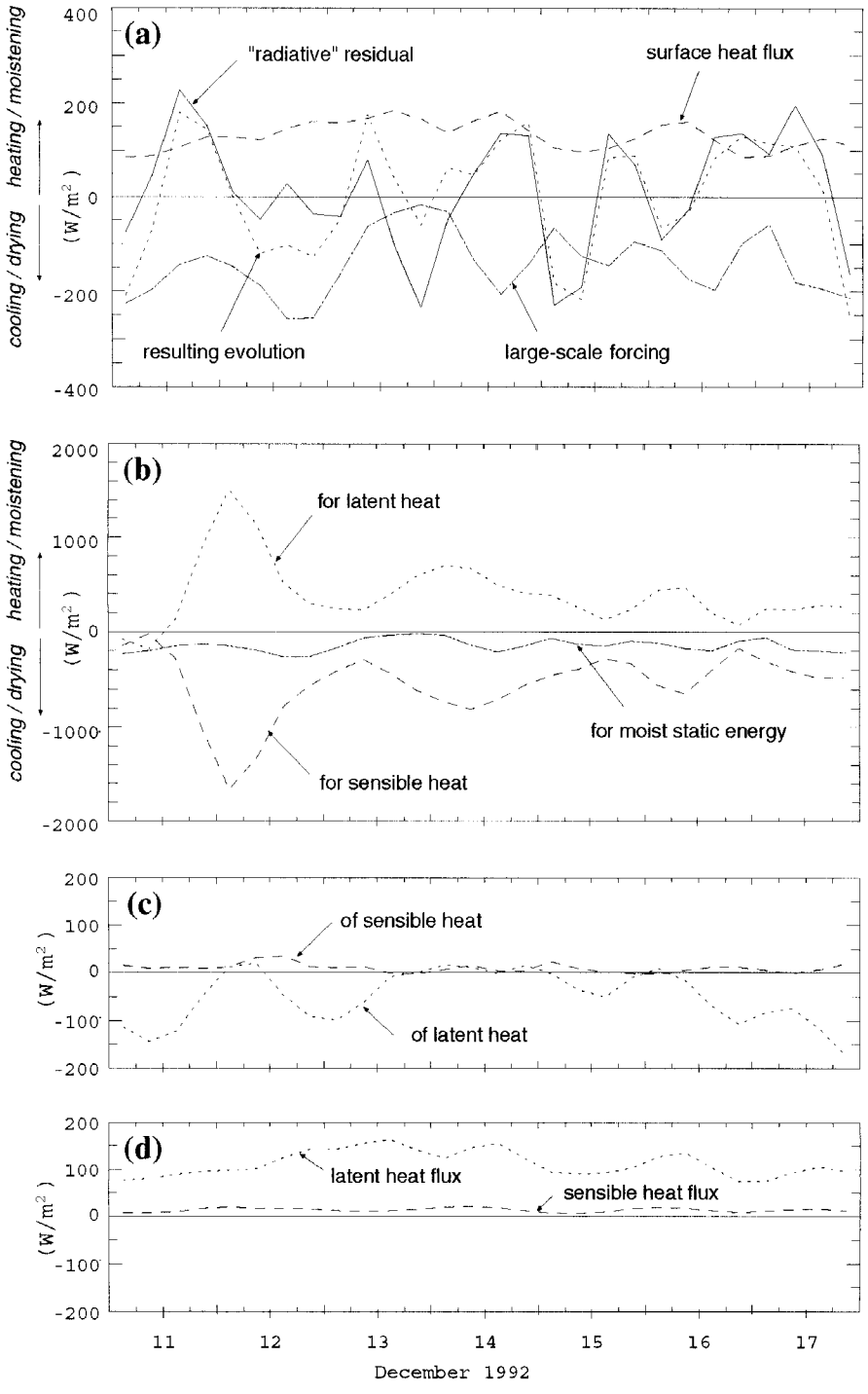

Figure 10. Vertically integrated IFA-mean thermodynamic budgets diagnosed from observations: (a) same as Fig. 9 except from observations, (b) large-scale cooling and moistening (sum of vertical and horizontal large-scale advection), (c) large-scale horizontal advection of temperature and moisture, and (d) surface sensible- and latent-heat fluxes. The time average is 6 h, centred on $(3 + 6n)$ h, and the vertical scales are all the same except for (b).

TABLE 1. SEVEN-DAY-MEAN VERTICALLY INTEGRATED THERMODYNAMIC BUDGETS DEDUCED FROM THE LARGE-SCALE OBSERVATIONS

	Dry static energy ($W\ m^{-2}$)	Moisture: $L_v*(q_v$budget) ($W\ m^{-2}$)	Moist static energy ($W\ m^{-2}$)
Large-scale horizontal advection	10	−50	−40
Large-scale vertical advection	−558	456	−102
Large-scale forcing (total)	−548	406	−142
Surface fluxes	13	117	130
Radiation	15	0	15

See text for definition of symbols.

the moist static energy budget (Eq. (2)). One must keep in mind, however, that Φ_R^{bud} corresponds to the 'radiative flux' that is actually in balance with the surface fluxes and the large-scale forcings diagnosed from observations, it does not result from any radiative calculations. The seven-day average of all budget terms is also given in Table 1.

The large-scale forcing on moist static energy results from much larger sensible- and latent-heat forcings which partly compensate each other (Fig. 10(b)) with seven-day-average values of -548 and 406 W m^{-2}, respectively. These large-scale forcings are primarily explained by large-scale vertical advection as the horizontal advection is an order of magnitude smaller (Fig. 10(c)). The horizontal advection is negligible for temperature (a result of a very uniform tropical-temperature field), but not for moisture. Most of the time, horizontal advection of moisture results in a drying of the atmosphere, thus partly balancing the oceanic evaporation. As noticed above, temporal fluctuations of LS(h) are complex. They are not in phase with large-scale cooling and moistening. In fact, minima of LS(h) (Fig. 10(a)) occur 5 to 10 h later than maxima of the large-scale cooling, and are coupled to maxima of large-scale horizontal advective drying (Fig. 10(c)). The temporal evolution of the moist static energy $\overline{\overline{h}}$ exhibits significant fluctuations with time. They mainly result from diurnal modulation of temperature (equivalent to $\approx$0.6 K of amplitude) coupled with more complex drying/moistening phases (not shown). The total surface heat flux (Fig. 10(a), dashed curve) is mainly due to the surface evaporation (Fig. 10(c)) and its temporal fluctuations are weak. This flux is closely matched in the model (Fig. 9, dashed line).

The deduced radiative flux Φ_R^{bud} also exhibits complex fluctuations that cannot be explained simply by the diurnal cycle. Moreover, Φ_R^{bud} tends to be positive or only slightly negative at night, except for the 13 and 14 December nights. This is especially obvious on the 16 December. At night, Φ_R^{bud} always contributes more than $+100$ W m^{-2}, equivalent to a warming of 1 K d^{-1} over the whole column. It is unlikely that such a heating actually occurred: for this night-time period, satellite data indicate a cloud cover less than 50%. Finally, it is important to notice that Φ_R^{bud} and Φ_R^{mod} have the same order of magnitude (seven-day-mean values are 15 W m^{-2} for both of them).

This analysis stresses high values of Φ_R both for the residual derived from observations and for the simulation. This result is in general agreement with the discussion of this term by Johnson and Ciesielski (2000) for the whole IOP. They also stressed the large range of uncertainties in the estimates of atmospheric radiative-heating rate as derived by various observational sources. Indeed, their estimate appears as one of the highest derived. The present analysis, focussing on a much smaller time-scale, also stresses a lack of consistency of Φ_R^{bud} over some periods with regard to the diurnal cycle of radiation, in agreement with the earlier finding of Emanuel and Zivkovic-Rothman (1999).

(*c*) *Radiative-forcing estimates from independent observational datasets*

At this stage, independent estimates of Φ_R derived from a collection of satellite data and surface radiative-flux measurements provide some insights into the possible range of values of Φ_R, and its diurnal features. The net atmospheric radiative flux, Φ_R^{obs}, is obtained as the difference between radiative fluxes at the top of the atmosphere (TOA) and the surface. Three independent data sources are used for the TOA radiative fluxes, hereafter referred to as 'Collins, ISCCP and Minnis'. Collins fluxes are derived from a combination of geostationary satellites and co-located high-altitude aircraft measurements (Collins *et al.* 1997, 2000). ISCCP fluxes are obtained with the 'Flux Cloud Technique' (Rossow and Zhang 1995; Zhang and Rossow 1995) as part of the International Satellite Cloud Climatology Project (ISCCP). Minnis fluxes are retrieved from the Geostationary Meteorological Satellite-4 narrowband radiances coupled with a calibration from pre-existing broadband measurements (Doelling *et al.*1999). The COARE IOP three-hourly mean values derived by Burks (1998) and Burks and Krueger (1999) from the Collins and Minnis datasets are used, together with the ISCCP dataset that has been weighted by area occupancy over the IFA; the resolution of the ISCCP dataset is 2.5° with 3 h sampling.

Estimates of the surface radiative fluxes (noted SRF) correspond to three-hour averages over five IFA surface stations (derived by Burks 1998; Burks and Krueger 1999), except for ISCCP data. In this latter case, surface radiative fluxes were retrieved with a radiative model. A complete description of this dataset can be found in Burks (1998).

Time series of the envelope of the three Φ_R^{obs} estimates (Collins+SRF, Minnis+SRF, ISCCP), together with Φ_R^{bud}, are shown in Fig. 11(a). The diurnal cycle of Φ_R^{obs} is obvious in these datasets, with a daytime amplitude of several hundreds of W m^{-2} as in the simulation (Fig. 9). This contrasts with Φ_R^{bud} temporal fluctuations (solid line). The width of this envelope also indicates significant uncertainties, especially during daytime. On average over the seven-day period, ISCCP data give the lowest atmospheric radiative-heating rate (with $\Phi_R^{obs} = -110$ W m^{-2}), Minnis TOA data coupled to surface measurements provide an intermediate value (-65 W m^{-2}) and Collins+SRF leads to the higher estimate (-12 W m^{-2}). This last estimate, however, is thought to be somewhat too large due to an underestimation of the short-wave (SW) upward flux at the TOA (Collins 1999, Personal communication). The difference between Collins+SRF and Minnis+SRF estimates is related to differences in the SW upward flux at the TOA, whereas the difference between ISCCP and Minnis+SRF estimates is due to different values of surface fluxes. The impact of these uncertainties is illustrated in Fig. 11(b). It shows that the temperature change due to atmospheric radiative processes varies from -6.6 K with ISCCP data to -0.7 K with Collins+SRF data; Φ_R^{bud} leads to an increase of $+0.7$ K.

(*d*) *Large-scale-forcing uncertainties*

Uncertainties in Φ_R^{bud} reveal those involved in diagnosing surface fluxes and large-scale forcings (assuming that IFA-mean moist static energy variations are correct). An estimation of IFA-mean surface fluxes is not straightforward: in particular it is difficult to aggregate local values because of their significant variability. However, Fig. 2 of Lin and Johnson (1996b) indicates that uncertainties in surface flux estimates are less than a few tens of W m^{-2}. So, the most probable candidate for explaining 6 h mean differences between Φ_R^{bud} and Φ_R^{obs} appears to be the large-scale forcing. As noticed above, the

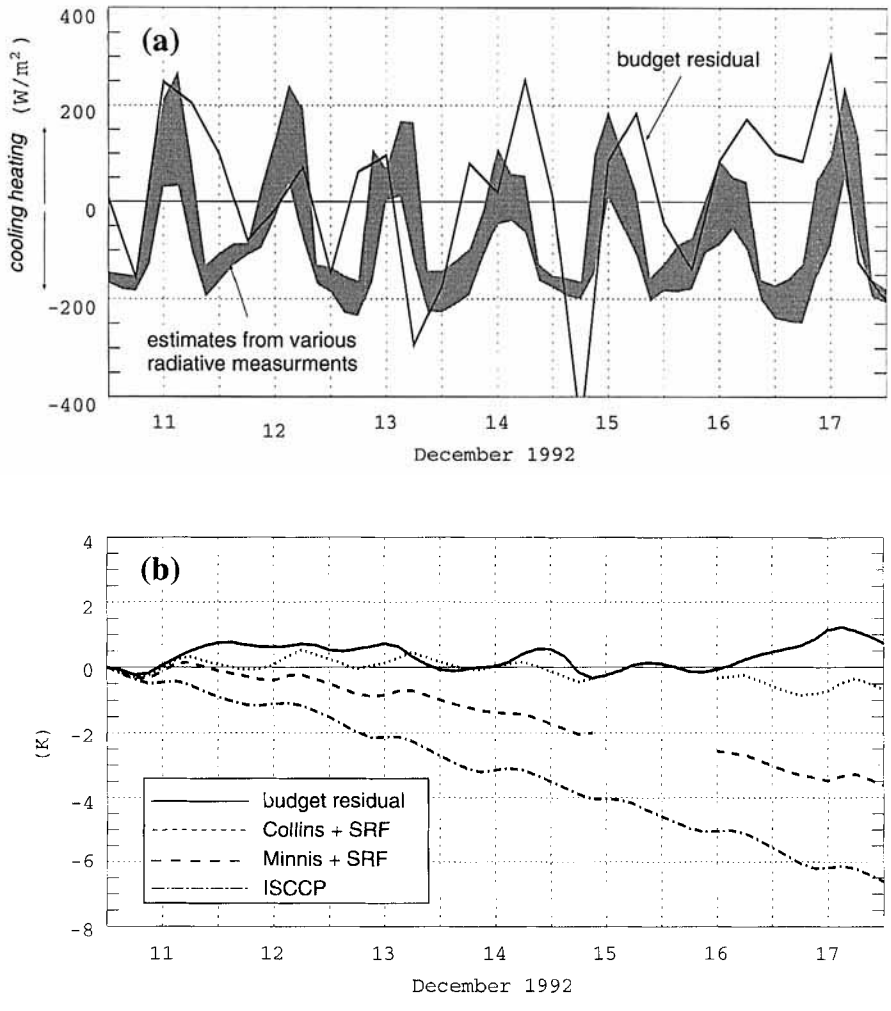

Figure 11. (a) Time series of IFA-mean net atmospheric radiative flux: envelope of Φ_R^{obs} minima and maxima obtained from Collins+SRF, Minnis+SRF and ISCCP datasets (grey shading) and as computed from the residual of large-scale budget Φ_R^{bud} (solid line). The sampling intervals are 6 h for Φ_R^{bud} (beginning at 12 UTC) and 3 h for Φ_R^{obs}. (b) Time series of column-mean temperature change due to radiation, calculated with Φ_R^{bud} (solid line), and the three Φ_R^{obs} estimates. 15 December is missing for Collins+SRF and Minnis+SRF in (b) because of a few missing values; for each of these two curves, it has been assumed that the 24 h slope on 15 December was equal to its slope averaged over the first four days.

large-scale forcing of moist static energy results from the imbalance between the large-scale forcings of temperature and moisture which have much larger amplitudes. Thus, a small uncertainty in one of these two large-scale tendencies will result in a noticeable uncertainty in the large-scale forcing of moist static energy. For example, a small error in the moisture budget alone will result in an error in the moist static energy, whereas it will only produce a second-order error in the rainfall estimate. However, it cannot be neglected for an analysis of simulated temperature and moisture. Xu and Randall (1996) found significant differences in terms of simulated temperature and moisture for two different large-scale advection datasets. However, they did not analyse the differences between the two datasets. It is the object of the following section to discuss why and

how large-scale-forcing uncertainties can affect the simulated temperature and moisture fields.

5. Sensitivity tests to possible sources of uncertainties

Several numerical tests have been performed with the model, in order to get some insight into the impact of some model changes and of uncertainties related to external forcings (Table 2). The simulation already presented will be designated as BASE.

Fig. 12(a) shows the vertical profile of the seven-day-mean difference between simulated and observed T, q_v and $\pi\theta_e$ for BASE. The simulated T is too weak by approximately 1 K and q_v too high by 0.5 to 1 g kg^{-1}. These biases tend to compensate but the resulting mean θ_e is still too high below 6 km, and too small above. These quantities are not significantly modified for a domain of half the size—experiment SIZE (Fig. 12(b)). Improvements induced by increasing the domain size are weak (see also Table 3). The most noticeable effect concerns water vapour, slightly closer to observations with a larger domain. Therefore, sensitivity experiments have been performed with a domain 256 km wide.

(*a*) *Sensitivity to ice fall speed*

The analysis presented in section 4 suggests that Φ_R^{mod} is too high. The most likely reason for this problem is to be found in the simulated cloud cover, as departure of temperature and moisture from observations could not explain more that a few W m^{-2}.

A comparison of the outgoing long-wave radiation (OLR) with satellite data provides valuable insights into the simulated cloud cover. Indeed, the estimates from the three satellite datasets are very close to each other, with seven-day-mean differences less than 5 W m^{-2}. Major fluctuations of OLR are associated with changes in the cloud cover (Fig. 13), increasing when clear-sky conditions prevail over the IFA (up to 230 W m^{-2}), then further decreasing when the IFA is almost entirely covered by clouds (down to 130 W m^{-2}). Consistent with previous findings, the OLR simulated in BASE is too weak (Fig. 13), with a seven-day-mean value of 152 W m^{-2} as against 190 W m^{-2} from satellite data. Fluctuations are also much weaker in the simulation, indicative of too high and persistent an upper-level cloud amount.

Two major reasons can explain these differences. First, there are still large uncertainties in ice-phase microphysical parametrizations, especially those related to ice nucleation and sedimentation. Second, as discussed by Wu *et al.* (1998), large-scale motions of ice hydrometeors mainly due to the formation of large iced anvils are not taken into account because they are very difficult to estimate from observations. This may create significant differences between simulated and observed OLR.

The experiment SED (Fig. 13) shows the control of the cloud cover on the OLR. This experiment is similar to SIZE, except for cloud-ice sedimentation. Partly based on Starr and Cox (1985), the formulation of ice fall speed has been modified to allow the particles to fall three times more rapidly. For BASE, ice-crystal mean terminal velocities typically do not exceed 35 cm s^{-1}. These values are relatively low as compared with those discussed in Wu *et al.* (1998) for instance. The maxima are of the order of 80 cm s^{-1} in SED. The resulting cloud cover is weaker, and simulated OLR agrees much better with observed—its mean value is now 194 W m^{-2}.

The cloud cover and OLR are improved in simulation SED. The rainfall rate also increases by 7%, coherent with the larger atmospheric radiative destabilization and surface heat fluxes (Table 3). However, the temperature is now much too low

TABLE 2. LIST OF SIMULATIONS

Simulation	Domain width	Ice sedimentation	Large-scale forcing
BASE	512 km	No increase	Normal
SIZE	256 km	No increase	Normal
SED	256 km	Increased	Normal
LST	256 km	Increased	Modified for T
LSQ	256 km	Increased	Modified for q
LST_2	256 km	Increased	Modified for T above 7 km
LSZ	256 km	No increase	Modified for T and q (as a function of height only)

See text for details of simulations and symbols.

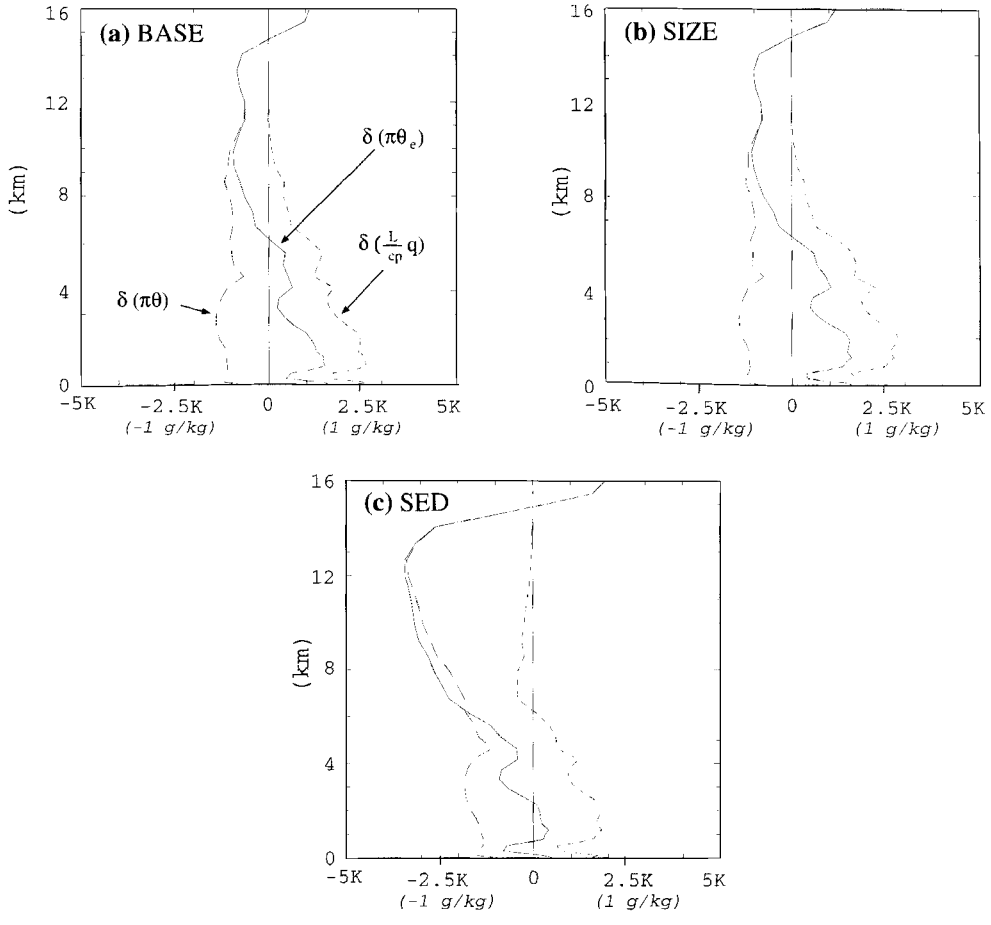

Figure 12. Seven-day-mean difference between simulated and observed temperature, moisture and equivalent potential temperature, for simulations (a) BASE, (b) SIZE and (c) SED: $(T^{\mathrm{mod}} - T^{\mathrm{obs}})$ (long dashes), $\frac{L_v}{c_p}(q_v^{\mathrm{mod}} - q_v^{\mathrm{obs}})$ (short dashes), $\pi(\theta_e^{\mathrm{mod}} - \theta_e^{\mathrm{obs}})$ (solid line). See text for explanation.

TABLE 3. SEVEN-DAY VERTICALLY INTEGRATED MEAN MOIST STATIC ENERGY BUDGETS. THE SMALL RESIDUAL DUE TO THE SUM OF MELTING AND FREEZING IS ADDED TO THE SURFACE FLUX $\Phi(h)_{srf}$.

	Moist static energy budget (W m^{-2})				Rainfall rate (mm day^{-1})
	$d\bar{\bar{h}}/dt$	Surface flux $\Phi(h)_{srf}$	Large-scale forcing LS(h)	Radiation Φ_R	
Simulations					
BASE	7	123	−131	15	16.9
SIZE	9	122	−131	18	16.8
SED	−33	134	−131	−36	18.0
LST	46	103	−6	−51	15.4
LSQ	59	106	−3	−44	19.8
LST_2	9	124	−72	−42	16.8
LSZ	−3	131	−153	19	15.6
Observations					
Large-scale budgets	3	130	−142	15	18.0
Collins+SRF	–	–	–	−12	–
ISCCP	–	–	–	−110	–
Minnis+SRF	–	–	–	−65	–

See text for details of experiments and symbols.

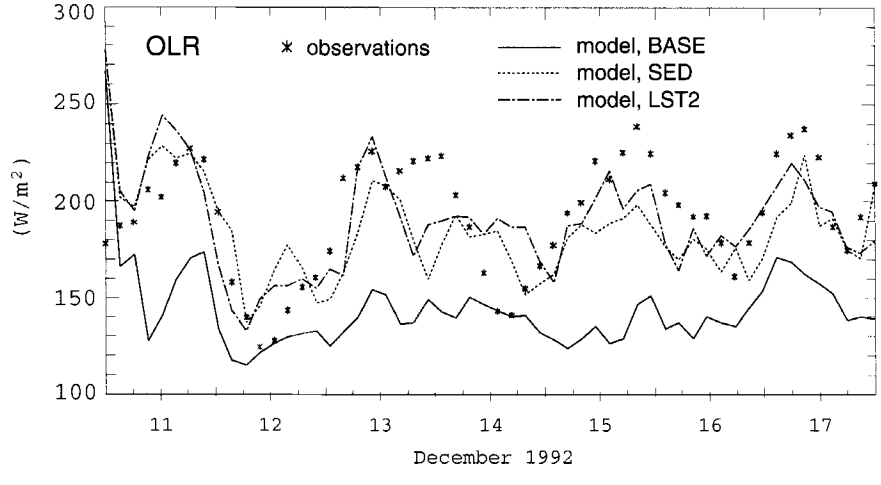

Figure 13. Time series of OLR observed (stars), and simulated for experiments BASE, SED and LST_2 (see text). The sampling interval is 3 h.

(Fig. 12(c)), especially above 6 km. This is better understood with the moist static energy budget (Table 3). The more realistic cloud cover of SED is associated with a large decrease of the net radiative-heating rate that is not balanced by the large-scale forcing (prescribed) nor by the modest increase of surface heat fluxes. As a result, the atmospheric moist static energy in SED has to be lower than in SIZE, which explains the lower temperatures in SED.

Comparison of seven-day-mean $\pi(\theta_e{}^{mod} - \theta_e{}^{obs})$ for experiments SIZE and SED (Figs. 12(b) and (c)) shows that their vertical structures are very close, i.e.

$$\frac{\partial \theta_e}{\partial z}(\text{SIZE}) \approx \frac{\partial \theta_e}{\partial z}(\text{SED}).$$

The same is true for vertical gradients of T and q_v. Thus, $\pi\theta_e{}^{mod}$ values differ by a mean value, approximately constant in the vertical (except above 10 km). The difference, of the order of 1 K, can be related to different intensities of the total external forcing on the moist static energy in SIZE and SED. For SIZE, below 6 km, θ_e is too low, suggesting a lack of convective activity.

(*b*) *Sensitivity to large-scale-advection uncertainties*

(i) *Possible causes of uncertainties.* The comparison of Φ_R^{obs} and Φ_R^{bud} (Fig. 11) suggests that mean Φ_R^{bud} is too high. If one assumes that this is due to large-scale-forcing uncertainties only, it implies that this forcing is too low (for $\overline{\overline{h}}$), either producing too much net dry cooling or not enough net moistening, or a combination of both. This information does not distinguish between temperature and moisture forcing, nor does it indicate how to distribute the uncertainties in the vertical. Observations provide useful guidance for this problem, as shown hereafter, but do not lead to a unique answer.

The large-scale forcing is the result of contributions from horizontal ('H') and vertical ('V') advection:

$$LS(\alpha) = LS_H(\alpha) + LS_V(\alpha).$$

As shown previously, $LS_H(T)$ is negligible due to extremely weak horizontal temperature gradients over the IFA region. So, if one assumes that uncertainties affect the temperature large-scale forcing, their origin is to be found in large-scale vertical advection of temperature. Then, as mean-IFA temperature vertical gradient derived from observations can be considered as a robust estimate, it follows that the uncertainties would concern the mean vertical mass-flux estimate.

In contrast with temperature, water-vapour horizontal gradient is not negligible. Under these weak wind conditions, $LS_H(q_v)$ mostly impacts the [3 km, 7 km] layer, with a maximum drying at 5 km coinciding with the height of the wind-speed maximum. This term is difficult to estimate because of the patchy structure of atmospheric moisture, and also because measurement uncertainties affect this process. If one assumes that existing uncertainties affect the moisture large-scale horizontal advection alone, this process would be responsible for less drying on average, in order to increase the net h large-scale forcing. This assumption would lead to the conclusion that uncertainties affecting $LS_H(q_v)$ are of the same order of magnitude as $LS_H(q_v)$.

Vertical advection of temperature and moisture are the dominant contributors to large-scale forcings. They are tightly coupled through the mean vertical velocity. As shown previously, large-scale vertical advection of h results from much larger temperature and moisture advection. So, it is not realistic to assume that uncertainties can result from *vertically integrated* mean vertical mass fluxes alone. In effect, this would lead to extremely different IFA-mean vertical velocity $\overline{W}_{ifa}$, not consistent with observed temporal fluctuations of convective activity, nor compatible with reasonable intensity of subsidence during suppressed periods.

A comparison of vertical gradients of temperature and moisture provides further information (Fig. 14). In effect, both are monotonic functions of height, but their contribution to the moist static energy vertical gradient are different. Three layers can be isolated. Between 1 and 3 km, an increase of $\overline{W}_{ifa}$ would lead to more moistening than cooling; the opposite occurs above 5 km. So, it is clear that the vertical structure of the uncertainties affecting $\overline{W}_{ifa}$ estimate can be important. For instance, an increase of $\overline{W}_{ifa}$ below 3 km enhances large-scale cooling and moistening with a net increase of the large-scale moist static energy forcing, whereas the opposite occurs above 5 km.

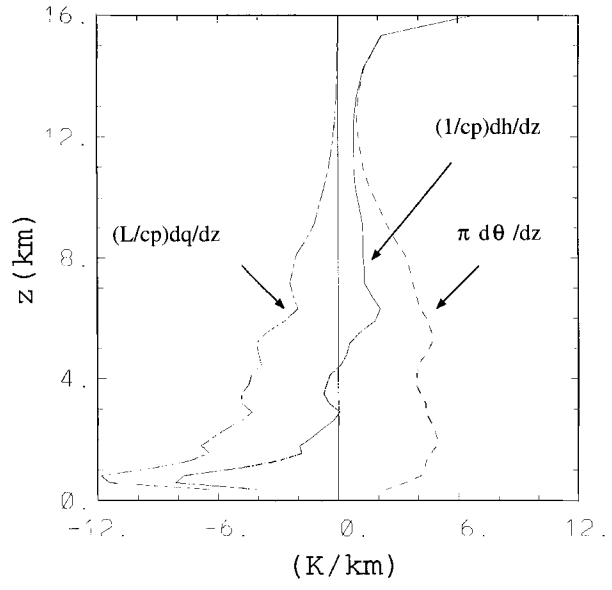

Figure 14. Seven-day IFA-mean vertical gradient of observed moist static energy h, temperature and moisture: $\frac{\partial h}{\partial z}$ (solid line), $\pi \frac{\partial \theta}{\partial z}$ (dotted line), $\frac{L_v}{c_p} \frac{\partial q_v}{\partial z}$ (dashed-dotted line). See text for explanation of symbols.

This analysis points out different possible causes of large-scale-forcing uncertainties, involving both mean vertical-velocity profile and large-scale horizontal advection of moisture. In the present case, an increase of vertically integrated large-scale forcing of moist static energy can be achieved through an increase of $\overline{W}_{\text{ifa}}$ below 3 km and/or a decrease of $\overline{W}_{\text{ifa}}$ above 5 km, modulated by horizontal large-scale advection of moisture.

(ii) *Sensitivity experiments.* The sensitivity of model thermodynamic fields to the intensity of the large-scale forcings is investigated with the following experiments (Table 2). In a first step, the difference $\Phi_{\text{R}}^{\text{bud}} - \Phi_{\text{R}}^{\text{obs}}$ as a function of time is used to modify the large-scale forcings of either temperature (simulation LST) or moisture (simulation LSQ), e.g. for temperature

$$\text{LS}(T)_{\text{new}} = \text{LS}(T) + \Phi_{\text{R}}^{\text{bud}} - \Phi_{\text{R}}^{\text{obs}}.$$

In this case, a simple correcting factor is applied to the whole vertical column. Otherwise, simulations LST and LSQ are similar to SED. The ISCCP values, corresponding to the larger atmospheric radiative-cooling rate (Fig. 11), are used to illustrate the most extreme case. The modifications of the large-scale forcings for these two experiments are shown in Fig. 15.

For both experiments LST and LSQ the temperature profile is better simulated (Figs. 16(a) and (b)), when compared to SED (Fig. 12(c)). At the same time, the evolution of OLR is close to the one found for SED (not shown). Though the simulated radiative cooling (Table 3) is larger than for SED (≈ -50 W m^{-2} for LST and LSQ as against -36 W m^{-2} for SED), it is still smaller than the ISCCP estimate. This increase is only partly compensated by the decrease of surface heat fluxes. As a result, the sum of the forcings acting on $\overline{\overline{h}}$ is much higher than in SED, so that the simulated $\overline{\overline{h}}$ is now too high, whereas it was too small for SED. For the two experiments LST

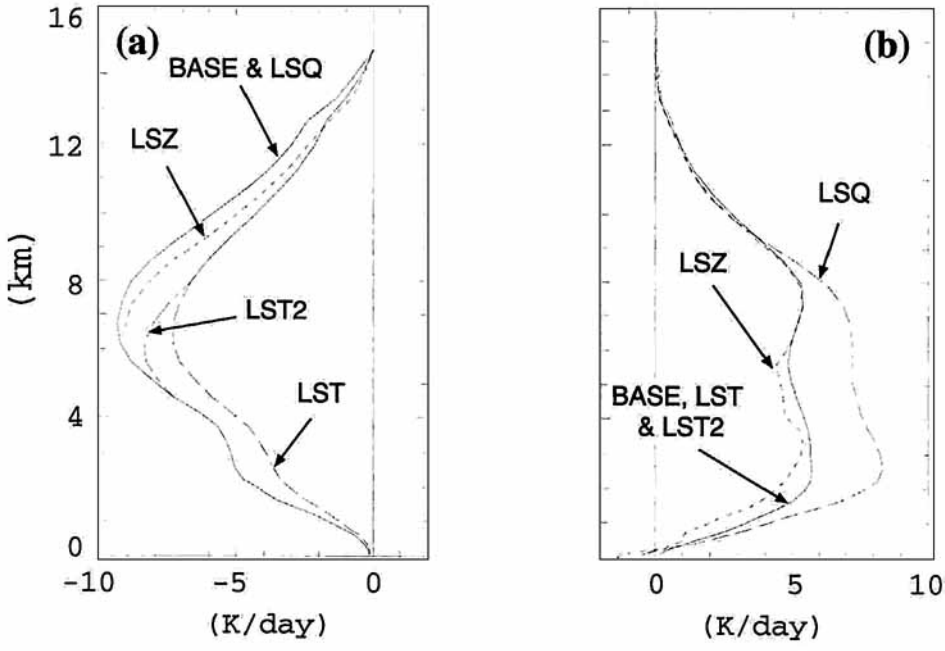

Figure 15. Seven-day-mean (a) large-scale cooling and (b) moistening, for the sensititivity experiments.

and LSQ, this also leads to a dramatic change of simulated moisture fields below 6 km (Figs. 16(a) and (b)). Rainfall rates respond to these modifications (Table 3) with significantly less precipitation when the large-scale destabilization is reduced (LST), and more precipitation when large-scale advection provides more moisture (LSQ).

The experiment LST_2 illustrates the magnitude of the modification of $LS(T)$ that is required in order to get *at the same time* temperature and moisture fields close to the ones in SIZE *and* an OLR in the same range as in SED. Experiment LST_2 is similar to LST except that the correction of the large-scale cooling is not applied over the whole column but only above 5 km, increasing linearly from 0 at 5 km to its value in LST at 7 km (Fig. 15). The residual radiative flux Φ_R^{bud} in equilibrium with this modified large-scale forcing lies in between the Minnis+SRF and Collins+SRF estimates, close to Φ_R^{mod} for the simulation SED. This would correspond to the assumption that large-scale-forcing uncertainties are associated with $\overline{W}_{ifa}$ in the upper levels, thus affecting mostly the large-scale forcing of temperature. As in LST, the temperature profile in LST_2 is largely improved in the upper levels as compared to SED (Fig. 16(e)) but the moisture field and rainfall rate stay close to the one in SIZE and the OLR is also close to the one in SED and to observations (Fig. 13).

A last experiment, LSZ, investigates the sensitivity of the simulation to the vertical structure of the large-scale forcing. Experiment LSZ is similar to SIZE (initial ice fall speed) except that the large-scale forcing is modified according to the seven-day-mean $(\theta_e{}^{mod} - \theta_e{}^{obs})$ profile. It consists of a decrease of h-forcing below 6 km, and an increase above. This modification, uniform in time, is applied to the moisture forcing below 6 km, and to the temperature forcing above (Fig. 15); it ranges from 0.5 to 1.5 K d^{-1}. This modification can be roughly interpreted as an increase of the large-scale horizontal advection of moisture coupled to a decrease in IFA-mean vertical velocity above 6 km.

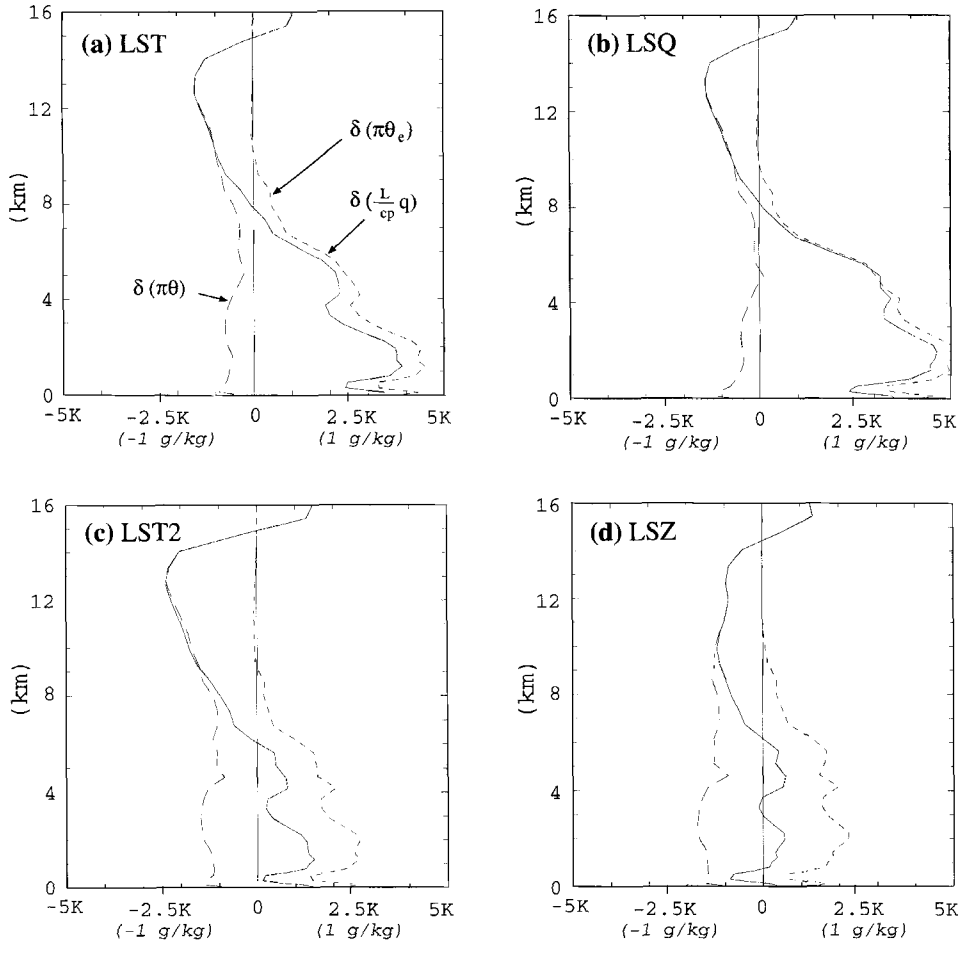

Figure 16. Same as Fig. 12 but for simulations (a) LST, (b) LSQ, (c) LST_2 and (d) LSZ (see text).

Seven-day-mean thermodynamic profiles resulting from the LSZ experiment, are shown in Fig. 16(d). Though the change of the large-scale-forcing profiles is small, it leads to a substantial improvement of moisture and θ_e below 6 km. Moreover, the mean vertical gradient of θ_e is much closer to observed.

6. Conclusion

Large-scale forcings of temperature and water vapour derived from observations (e.g. Lin and Johnson 1996a) are often used to evaluate cloud parametrizations via a single-column model. In the present study, a cloud-resolving model has been used in the same way except for explicitly simulating the convective activity. The 20–26 December 1992 period, corresponding to the onset of a westerly wind burst over the COARE area, was chosen as a case of the GCSS WG4 model intercomparison project (Krueger *et al.* 1996). Here, we focussed on a period of intense precipitation too (10–17 December 1992), but one which occurred prior to this WWB. The wind shear was weak compared to the one for the 20–26 December 1992 period, and cloud systems also appear as more convective (as opposed to stratiform) with larger moisture convective transports.

A comparison of simulated precipitation, apparent heat source and moisture sink with observations shows that the model reproduces these convective features fairly well. Agreement between simulated and observed temperature and moisture is more challenging. The simulation exhibits a slight cold bias (≈ -1 K over seven days), coupled below 5 km with an apparently moist bias—a clear evaluation of the simulated humidity is actually difficult, because moisture measurements are affected by a significant dry bias (Zipser and Johnson 1998; Cole and Miller 1999). Time variations of these fields are reasonably well captured by the model.

A further evaluation of model thermodynamic fields and their relations with external-forcings accuracy has been handled with the help of the *moist static energy budget*, expressing the balance between the three 'external forcings' (large-scale forcing, surface heat flux and net atmospheric radiative flux Φ_R) together with independent radiative datasets. Simulated surface heat fluxes are actually close to observed, but simulated Φ_R temporal fluctuations significantly depart from those of the residual Φ_R^{bud} deduced from large-scale budgets. In practice, although large-scale budgets do not directly include a computation of Φ_R, it appears as a residual in the vertically integrated moist static energy budget, and corresponds to the net atmospheric radiative-heating rate that is in equilibrium with the large-scale forcings and surface fluxes deduced from observations. For this seven-day period, Φ_R^{bud} values seemed too high as compared to independent datasets including satellite and surface observations (Rossow and Zhang 1995; Burks and Krueger 1999). It seems likely that this problem is related to inherent uncertainties in the large-scale-forcing estimates. The simulated Φ_R exhibits a strong diurnal cycle that agrees well with the datasets derived from satellite observations. Simulated Φ_R was, however, found sensitive to the fall speed of ice crystals used in the CRM. More realistic values of simulated OLR and Φ_R are obtained when the cloud cover is reduced through increasing the fall speed of ice crystals. However, in that case, because the mean value of simulated Φ_R is lower than Φ_R^{bud}, the simulated moist static energy is significantly changed. Indeed, as far as the simulated Φ_R not agreeing with Φ_R^{bud}, it appears, as previously shown by Emanuel and Zivkovic-Rothman (1999), that a correct simulation of both T and q_v is elusive when surface heat fluxes are correctly reproduced by the model. Otherwise a bias necessarily develops, affecting temperature and/or moisture fields.

Additional experiments investigated the sensitivity of model results to the mean intensity of external moist static energy forcings. They show that the thermodynamic fields change with the intensity of large-scale forcings, but their vertical gradients are very similar from one experiment to the other. Thus, these gradients and how they depart from observed appear as robust features characterizing the model behaviour, independently of uncertainties in the intensity of the large-scale forcings.

In this respect, the vertical structure of the large-scale forcings is crucial, as minor changes of these profiles have been found to significantly impact on the vertical structures of T and q_v, illustrating the tight interactions between the large-scale motions and the convective activity in determining atmospheric stratification, as pointed out by Mapes (1997).

These sensitivity tests point out three important issues:

(i) The knowledge of uncertainties in external forcings is crucial if one wants to get a relevant evaluation of simulated temperature and moisture fields, as 'correct' fields of temperature and moisture can hide model errors matching observation uncertainties.

(ii) It is important to use independent sources of data for an advanced evaluation of both observations and models.

(iii) The vertical structures of the large-scale forcing play a crucial role, as small changes of these profiles have significant impact on T and q_v.

These issues also highlight the central role of moist static energy diagnostics that could be more systematically used for this kind of test. Differences between Φ_R^{bud} and Φ_R^{obs} give valuable insights into the level of uncertainties we are faced with. It is important to note that this finding does not only account for CRM tests, but also for any SCM experiment. Thus, for this type of 'SCM-like' framework, it seems important to jointly analyse vertically integrated h budget deduced from large-scale observations and simulated when one wants to evaluate simulated T and q_v with observations. In addition, the vertical structure of moist static energy appears as a relevant quantity that could be more widely used for an advanced evaluation of models.

ACKNOWLEDGEMENTS

The authors want first to thank D. Johnson and colleagues for the production and distribution of their data. S. Krueger and J. Burks who aggregated Collins, Minnis and surface dataset over the IFA of COARE are gratefully acknowledged, so are W. Collins for helpful discussion, and P. Kucera who provided useful help with the radar data in the early stage of this study. The authors thank ISCCP, Goddard Institute for Space Studies and the Distributed Active Archive Center (Code 902.2) at the Goddard Space Flight Center Greenbelt, M 20771 for the production and distribution of these data, respectively. These activities are sponsored by NASA's Mission to Planet Earth Program. The authors also thank two anonymous reviewers and the editorial board. Finally, C. Kaufman and M. A. Pikkonen are acknowledged for editing the manuscript. Part of this research was realized during the visit of the first author to the National Center for Atmospheric Research.

REFERENCES

Balaji, V. and Redelsperger, J.-L. 1996 Sub-gridscale effects in mesoscale deep convection: Initialisation, organization and turbulence. *Atmos. Res.*, **40,** 339–381

Bougeault, P. 1985 A simple parameterization of the large-scale effects of cumulus convection. *Mon. Weather Rev.*, **113,** 2108–2121

Browning, K. A., Betts, A., Jonas, P. R., Kershaw, R., Manton, M., Miller, M., Moncrieff, M. W., Sundqvist, H., Tao, W. K., Tiedtke, M., Hobbs, P. V., Mitchell, J., Raschke, E., Stewart, R. E. and Simpson, J. 1993 The GEWEX cloud system study (GCSS). *Bull. Am. Meteorol. Soc.*, **74,** 387–399

Burks, J. E. 1998 'Radiative fluxes and heating rates during TOGA COARE over the intensive flux array'. MS thesis, Department of Meteorology, University of Utah (available from Department of Meteorology, 819 Browning Bldg., University of Utah, Salt Lake City, UT 84112)

Burks, J. E. and Krueger, S. K. 1999 'Radiative fluxes and heating rates during TOGA COARE over the intensive flux array'. Pp. 773–775 in Preprints of 23rd conference on hurricanes and tropical meteorology, 10–15 January 1999, Dallas, Texas, USA

Caniaux, G., Redelsperger, J.-L. and Lafore, J.-P 1994 A numerical study of the stratiform region of a fast-moving squall line. Part I: General description and water and heat budgets. *J. Atmos. Sci.*, **51,** 2046–2074

Ciesielski, P. E., Hartten, L. M. and Johnson, R. H. 1997 Impacts of merging profiler and rawisonde winds on TOGA COARE analyses. *J. Atmos. Oceanic Technol.*, **14,** 1264–1279

Cole, H. and Miller, E. 1999 'Correction and re-calculation of humidity data from TOGA COARE radiosondes and development of humidity correction algorithms for global radiosondes data'. Pp. 139–141 in Proceedings of the COARE-98 conference, 7–14 July 1998, Boulder, CO, WCRP-107, WMO/TD No. 940

Collins, W. D., Bucholtz, A. and Valero, F. P. 1997 'Derivation of top of atmosphere fluxes from geostationary satellites using high altitude aircraft measurements: results from COARE and CEPEX'. Pp. 198–202 in Preprints of ninth conference on atmospheric radiation, 2–7 February 1997, Long Beach, CA, USA, American Meteorological Society

Collins, W. D., Bucholtz, A., Lubin, D., Flateau, P., Valero, F. P. J., Weaver, C. P. and Pilewskie, P. 2000 Determination of surface heating by clouds in the central equatorial Pacific from surface and satellite measurements. *J. Geophys. Res*, **105,** 14807–14821

Doelling, D. R., Minnis, P., Palikonda, R. and Spangenberg, D. A. 1999 'Validation of TOA broadband fluxes derived fom GMS during TOGA/COARE'. Pp. 241–242 in Proceedings of the COARE-98 Conference, 7–14 July 1998, Boulder, CO, USA, WCRP-107, WMO/TD No. 940

Ebert, E. and Curry, J. A. 1992 A parameterization of ice cloud optical properties for climate models. *J. Geophys. Res.*, **97,** 3831–3836

Ebert, E. and Manton, M. J. 1998 Performance of satellite rainfall estimation algorithms during TOGA COARE. *J. Atmos. Sci.*, **55,** 1537–1557

Emanuel, K. A. and Zivkovic-Rothman, M. 1999 Development and evaluation of a convection scheme for use in climate models. *J. Atmos. Sci.*, **56,** 1766–1782

Del Genio, A. D., Yao, M. S., Kovari, W and Lo, K. K.-W. 1996 A prognostic cloud water parameterization for global climate models. *J. Climate*, **9,** 270–304

Godfrey, J. S., Houze Jr., R. A., Johnson, R. H., Lukas, R., Redelsperger, J.-L., Sumi, A. and Weller, R. 1998 Coupled Ocean–Atmosphere Response Experiment (COARE): An interim report. *J. Geophys. Res.*, **103(C7),** 14395–14450

Grabowski, W. W., Wu, X. and Moncrieff, M. W. 1996 Cloud resolving modeling of tropical cloud systems during phase III of GATE. Part I: Two-dimensional experiments. *J. Atmos. Sci.*, **53,** 3684–3709

Grabowski, W. W., Wu, X., Moncrieff, M. W. and Hall, W. D. 1998 Cloud resolving modeling of cloud systems during phase III of GATE. Part II: Effects of resolution and the third spatial dimension. *J. Atmos. Sci.*, **55,** 3264–3282

Gregory, D. 1997 Sensitivity of general circulation models performance to convective parameterization. Pp. 463–482 in *The physics and parameterization of moist atmospheric convection*, NATO ASI series C, Volume 505, Kluwer Academic Publishers, Amsterdam

Gregory, D. and Miller, M. J. 1989 A numerical study of the parametrization of deep tropical convection. *Q. J. R. Meteorol. Soc.*, **115,** 1209–1241

Guichard, F., Redelsperger, J.-L. and Lafore, J.-P. 1996 The behaviour of a cloud ensemble in response to external forcings. *Q. J. R. Meteorol. Soc.*, **122,** 1043–1073

1997a 'Cloud resolving modelling and the impact of physical parametrizations for several cloud systems observed during TOGA-COARE'. Pp. 357–362 in Proceedings of WMO Workshop: Measurement of cloud properties for forecasts of weather, air quality and climate, 23–27 June 1997, Mexico City, Mexico, WMP report No. 30

Guichard, F., Lafore, J.-P. and Redelsperger, J.-L. 1997b Thermodynamical impact and internal structure of a tropical convective cloud system. *Q. J. R. Meteorol. Soc.*, **123,** 2297–2324

Guichard, F., Parsons, D. and Miller, E. 2000 Thermodynamical and radiative impact of the correction of sounding humidity bias in the tropics. *J. Climate* (in press)

Hartmann, D. L., Hendon, H. H., and Houze Jr., R. A. 1984 Some implications of the mesoscale circulations in tropical cloud clusters for large-scale dynamics and climate. *J. Atmos. Sci.*, **41,** 113–121

Johnson, R. H. and Ciesielski, P. E. 2000 Rainfall and radiative heating rates from TOGA-COARE atmospheric budgets. *J. Atmos. Sci.*, **57,** 1497–1514

Krueger, S. K. 1997 'A GCSS intercomparison of Cloud-Resolving Models based on TOGA COARE observations'. Pp. 113–127 in Proceedings of ECMWF workshop: New insights and approaches to convective parameterization, 4–7 Nov 1997, Reading, UK

Krueger, S. K., Gregory, D., Moncrieff, M. W., Redelsperger, J.-L. and Tao, W.-K.	1996	GCSS Working Group 4:Technical report of the First Cloud-Resolving Model intercomparison Project. Case 2. GEWEX Cloud System Study Group (available at http://www.met.utah.edu/skrueger/gcss/case2submit.html)
Lafore, J.-P., Redelsperger, J.-L. and Jaubert, G.	1988	Comparison between a three-dimensional simulation and doppler radar data of a tropical squall line: Transport of mass, momentum, heat and moisture. *J. Atmos. Sci.*, **45,** 3483–3500
Li, X., Sui, C.-H., Lau, K.-M. and Chou, M.-D.	1999	Large-scale forcing and cloud–radiation interaction in the tropical deep convective regime. *J. Atmos. Sci.*, **56,** 3028–3042
Lin, X. and Johnson, R. H.	1996a	Heating, moistening and rainfall over the western Pacific warm pool during TOGA COARE. *J. Atmos. Sci.*, **53,** 3367–3383
	1996b	Kinematic and thermodynamical characteristics of the flow over the western Pacific warm pool during TOGA COARE. *J. Atmos. Sci.*, **53,** 695–715
Lord, S. J.	1982	Interaction of cumulus cloud ensemble with the large-scale environment. Part III: Semi-prognostic test of the Arakawa–Schubert cumulus parameterization. *J. Atmos. Sci.*, **39,** 88–103
Lucas, C. and Zipser, E. J.	2000	Environmental variability during TOGA COARE. *J. Atmos. Sci.*, **57,** 2333–2350
Mapes, B.	1997	Equilibrium vs. activation control of large scale variations of tropical deep convection. Pp. 321–358 in *The physics and parameterization of moist atmospheric convection,* NATO ASI series C, Volume 505, Kluwer Academic Publishers, Amsterdam
Miloshevich, L. M., Vömel, H., Paukkunen, A., Heymsfield, A. J. and Oltmans, S. J.	2000	Characterization and correction of relative humidity measurements from Vaisala rs80-a radiosondes at cold temperatures. *J. Atmos. Oceanic Technol.* (in press)
Moncrieff, M. W., Krueger, S. K., Gregory, D., Redelsperger, J.-L. and Tao, W.-K.	1997	GEWEX Cloud System Study (GCSS) Working Group 4: Precipitating convective cloud systems. *Bull. Am. Meteorol. Soc.*, **78,** 831–844
Morcrette, J.-J.	1991	Radiation and cloud radiative properties in the European Centre for Medium-Range Weather Forecasts forecasting system. *J. Geophys. Res.*, **96,** 9121–9132
Redelsperger, J.-L. and Guichard, F.	1996	'Detailed analysis of cloud systems observed during TOGA COARE: simulations forced and unforced by the large scale motions'. Pp. 58–76 in Proceedings of ECMWF workshop, New insights and approaches to convective parameterization, 4–7 Nov 1997, Reading, UK
Redelsperger, J.-L. and Lafore, J.-P	1994	Non-hydrostatic simulations of a cold front observed during the FRONTS 87 experiment. *Q. J. R. Meteorol. Soc.*, **120,** 519–555
Redelsperger, J.-L. and Sommeria, G.	1986	Three-dimensional simulation of a convective storm: Sensitivity studies on subgrid parameterisation and spatial resolution. *J. Atmos. Sci.*, **43,** 2619–2635
Redelsperger, J.-L., Guichard, F. and Mondon, S.	2000a	A parameterization of mesoscale enhancement of surface fluxes for large-scale models. *J. Clim.*, **13,** 402–421
Redelsperger, J.-L., Brown, P. R. A., Guichard, F., Hoff, C., Kawasima, M., Lang, S., Montmerle, T., Nakamura, K., Saito, K., Seman, C., Tao, W. K. and Donner, L. J.	2000b	A GCSS model intercomparison for a tropical squall line observed during TOGA-COARE. I: Cloud-resolving models. *Q. J. R. Meteorol. Soc.*, **126,** 823–863
Rossow, W. B. and Zhang, Y.-C.	1995	Calculation of surface and top-of-the-atmosphere radiative fluxes from physical quantities based on ISCCP datasets, Part II: Validation and first results. *J. Geophys. Res.*, **100,** 1167–1197
Short, D. A., Kucera, P. A., Ferrier, B. S., Gerlach, J. C., Rutledge, S. A. and Thiele, O. W.	1997	Shipboard radar rainfall patterns within the TOGA COARE IFA. *Bull. Am. Meteorol. Soc.*, **78,** 2817–2836
Smith, E.-A. and Shi, L.	1992	Surface forcing of the infrared cooling profile over the Tibetan plateau. Part I: Influence of relative longwave radiative heating at high altitude. *J. Atmos. Sci.*, **49,** 805–822

Sommeria, G. 1976 Three-dimensional simulation of turbulent processes in an undisturbed trade wind boundary layer. *J. Atmos. Sci.*, **33,** 216–241

Soong, S.-T and Tao, W.-K. 1980 Response of deep tropical cumulus clouds to mesoscale processes. *J. Atmos. Sci.*, **37,** 2016–2034

Starr, D. O'. C. and Cox, S. K. 1985 Cirrus clouds. Part I: A cirrus cloud model. *J. Atmos. Sci.*, **42,** 2263–2281

Thompson, R. M., Payne, S. W., Ricker, E. E. and Reed, R. J. 1979 Structure and properties of synoptic-scale wave disturbances in the Intertropical Convergence Zone of the eastern Atlantic. *J. Atmos. Sci.*, **36,** 53–72

Tiedtke, M. 1988 Parameterization of cumulus convection in large-scale models. Pp. 375–431 in *Physically-based modelling and simulation of climate and climatic change—Part I.* Ed. M. E. Schlesinger, Kluwer Academic Publishers, Amsterdam

Webster, P. J. and Lukas, R. 1992 TOGA COARE: the coupled ocean–atmosphere response experiment. *Bull. Am. Meteorol. Soc.*, **73,** 1377–1416

Weller, R. A. and Anderson, S. P. 1996 Surface meteorology and air–sea fluxes in the Western Equatorial Pacific warm pool during the TOGA Coupled Ocean-Atmosphere Response Experiment. *J. Climate*, **9,** 1959–1990

Wu, X., Grabowski, W. W. and Moncrieff, M. W. 1998 Long-term behaviour of cloud systems in TOGA COARE and their interactions with radiative and surface processes. Part I: Two-dimensional modeling study. *J. Atmos. Sci.*, **55,** 2693–2714

Wu, X., Hall, W. D., Grabowski, W. W., Moncrieff, M. W., Collins, W. D. and Kiehl, J. T. 1999 Long-term behaviour of cloud systems in TOGA COARE and their interactions with radiative and surface processes. Part II: Effects of ice microphysics and cloud–radiation interaction. *J. Atmos. Sci.*, **56,** 3177–3195

Xu, K.-M. and Randall, D. A. 1996 Explicit simulation of cumulus ensembles with the GATE phase III data: comparison with observation. *J. Atmos. Sci.*, **53,** 3710–3735

Zhang, Y.-C. and Rossow, W. B. 1995 Calculation of surface and top-of-the-atmosphere radiative fluxes from physical quantities based on ISCCP datasets. Part I: Method and sensitivity to input data uncertainties. *J. Geophys. Res.*, **100,** 1149–1165

Zipser, E. J. and Johnson, R. H. 1998 'Systematic errors in radiosonde humidities: A global problem?'. Pp. 72–73 in Preprints of the tenth AMS symposium on measurements, observations and instrumentation, 11–16 January 1998, Phoenix, Az. American Meteorological Society